A Joint Probability Density–Based Decomposition of Turbulence in the Atmospheric Boundary Layer

MARIA J. CHINITA

Faculdade de Ciências, Instituto Dom Luiz, Universidade de Lisboa, Lisbon, Portugal, and Jet Propulsion Laboratory, California Institute of Technology, Pasadena, California

GEORGIOS MATHEOU

Department of Mechanical Engineering, University of Connecticut, Storrs, Connecticut

JOÃO TEIXEIRA

Jet Propulsion Laboratory, California Institute of Technology, Pasadena, California

ABSTRACT

In convective flows, vertical turbulent fluxes, covariances between vertical velocity and scalar thermodynamic variables, include contributions from local mixing and large-scale coherent motions, such as updrafts and downdrafts. The relative contribution of these motions to the covariance is important in turbulence parameterizations. However, the flux partition is challenging, especially in regions without convective cloud. A method to decompose the vertical flux based on the corresponding joint probability density function (JPD) is introduced. The JPD-based method partitions the full JPD into a joint Gaussian part and the complement, which represent the local mixing and the large-scale coherent motions, respectively. The coherent part can be further divided into updraft and downdraft parts based on the sign of vertical velocity. The flow decomposition is independent of water condensate (cloud) and can be applied in cloud-free convection, the subcloud layer, and stratiform cloud regions. The method is applied to large-eddy simulation model data of three boundary layers. The results are compared with traditional cloud and cloud-core decompositions and a decaying scalar conditional sampling method. The JPD-based method includes a single free parameter and sensitivity tests show weak dependence on the parameter values. The results of the JPD-based method are somewhat similar to the cloud-core and conditional sampling methods. However, differences in the relative magnitude of the flux decomposition terms suggest that an objective definition of the flow regions is subtle and diagnosed flow properties like updraft characteristics depend on the sampling method. Moreover, the flux decomposition depends on the thermodynamic variable and convection characteristics.

1. Introduction

In weather and climate models the time evolution of scalar variables depends on the turbulent flux divergence and the combination of advective tendencies and diabatic processes, that is,

$$\frac{\partial \overline{\phi}}{\partial t} = -\frac{\partial \overline{u'_j \phi'}}{\partial x_j} + F_\phi, \tag{1}$$

where $\overline{\phi}$ is an ensemble-averaged scalar variable and $\overline{u'_j \phi'}$ its turbulent fluxes. Primes denote fluctuations with respect to the ensemble mean $\overline{\phi}$:

$$\phi = \overline{\phi} + \phi'. \tag{2}$$

For model grid resolutions much larger than the characteristic flow scales, the horizontal gradients of the turbulent fluxes are negligible and the dominant turbulent transport contribution is due to the vertical gradients of $\overline{w'\phi'}$. In convective conditions the propensity of turbulence to organize into large-scale coherent motions can be modeled by partitioning the vertical turbulent flux into contributions from local turbulent mixing and coherent motions (Chatfield and Brost 1987; Randall et al. 1992; Siebesma and Cuijpers 1995; Hourdin et al. 2002; Soares et al. 2004; Siebesma et al. 2007; Rio and Hourdin 2008; Pergaud et al. 2009; Angevine et al. 2010; Suselj et al. 2013):

Corresponding author: Maria J. Chinita, mariajoaochinita@gmail.com

$$\overline{w'\phi'} = -K\frac{\partial\overline{\phi}}{\partial z} + \overline{w'\phi'}_c, \tag{3}$$

where the first term on the right-hand side (rhs) represents the local mixing parameterized by the eddy-diffusivity assumption using a scalar coefficient K and the second term represents the ascending motions that can have sufficient kinetic energy to rise counter to the mean buoyancy gradient near the top of the boundary layer. Even though (3) is well defined and physically justified, partitioning the fluid motions into local and coherent-motion transport and mixing is challenging because of the random multiscale character of turbulence. Figure 1a shows an example of coherent structures in a dry convective boundary layer. Thermals are composed of eddies of various sizes, thus their sampling is challenging.

The decomposition into local and coherent motion contributions can be easily computed in the cloud layer of shallow cumulus convection (Siebesma and Cuijpers 1995) where the cloud, or a cloud subset such as the cloud core, can define the updraft. However, such decompositions cannot be performed in the subcloud layer, which is critical for parameterizations because cloud-topped updrafts emanate from this layer. Also, many coherent motions can contribute to the vertical flux but do not rise sufficiently high to form cloud. Moreover, in instances of stratiform cloud (e.g., stratocumulus) or detrained saturated air (e.g., anvils) the cloudy part of the atmosphere does not faithfully represent the coherent motions.

Several coherent motion and updraft sampling methods based on vertical velocity and thermodynamic variables have been used and evaluated in dry convective boundary layers, for example, Williams and Hacker (1992), Berg and Stull (2004) and Siebesma et al. (2007), see also discussion and further references in Couvreux et al. (2010). To overcome the limitations of coherent motion identification based on the vertical velocity and/or thermodynamic variables, Couvreux et al. (2010) introduced a sampling method based on a decaying scalar (tracer) emanating from the surface. The decay rate, which depends on the concentration and a fixed time scale (i.e., ϕ/τ) ensures that the scalar will not accumulate outside the updrafts. In other words, high concentrations are expected to correspond to active updrafts that are continuously replenished from the surface.

Figure 1b shows a snapshot of such a decaying tracer in a dry convective boundary layer. For this case, the decaying scalar and potential temperature are well correlated and the scalar marks the updraft structure. For comparison, Fig. 1c shows conditional sampling

based on the 95th percentile of the vertical velocity. Some of the limitations of identifying updrafts based on vertical velocity are discernible. For instance, regions with low values of potential temperature, which are not expected to be part of the updraft, are selected; and a large number of small disconnected regions are present.

The use of a tracer to conditionally sample the flow (Couvreux et al. 2010) has many advantages and is consistent with the cloud-based sampling of Siebesma and Cuijpers (1995). However, such methods require the integration of additional scalar variables in numerical models, therefore are not applicable to preexisting model output or observational data. Furthermore, the conditional sampling depends on several parameters and the results are sensitive to the parameter thresholds. Further details are discussed in section 4 and the appendix.

A method based on the joint probability density functions (JPDs) of vertical velocity with temperature and humidity, is developed to address the limitations of conditional sampling based on flow variables and/or additional scalar tracers. The JPD encapsulates the full statistical description of the fields (i.e., all statistical moments can be computed from the JPD). Accordingly, probability density functions (PDFs) are often used for analysis and modeling of convection (e.g., Wyngaard and Moeng 1992; Wang and Stevens 2000; Golaz et al. 2002; Larson and Golaz 2005; Bogenschutz and Krueger 2013). Previous studies have used joint Gaussians to approximate vertical velocity–scalar JPDs (Wyngaard and Moeng 1992) or temperature–humidity JPDs (Sommeria and Deardorff 1977; Berg and Stull 2004).

The character of the nonlocal mixing encapsulated in the flux decomposition in (3) manifests in the JPD as long "tails" corresponding to high absolute values of vertical velocities and dissimilar thermodynamic variable values (e.g., Wang and Stevens 2000; Neggers et al. 2002). Accordingly, in convective flows JPDs deviate from Gaussian distributions (Schumacher 2009). Even though the long non-Gaussian tails correspond to a small volume fraction of the flow and may not contribute significantly to mean quantities, they can have large contributions to the covariances (Siebesma and Cuijpers 1995; Wang and Stevens 2000). The present method takes advantage of this dual nature of the JPD. That is, the JPD is divided into two parts: a joint-Gaussian that approximates the bulk of the JPD near its peak and the remainder that represents the coherent motions. The coherent motion part can be further partitioned into updraft and downdraft contributions based on the sign of the vertical velocity.

Presently, only vertical fluxes are considered because the focus is on turbulence parameterization [e.g., (3)].
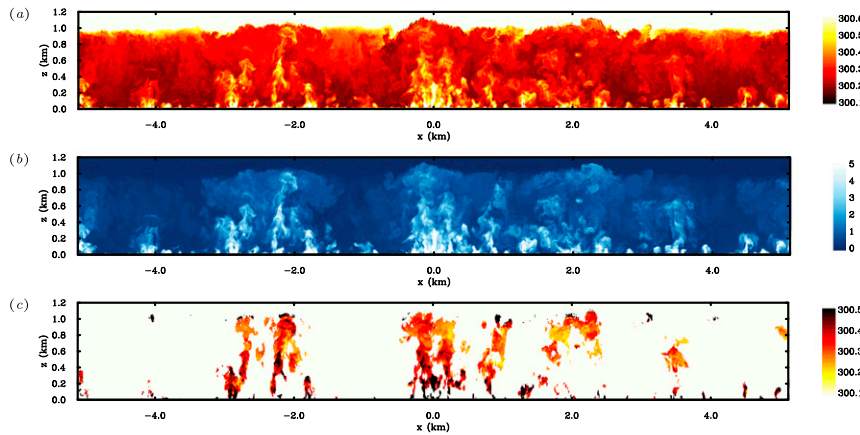
FIG. 1. (a) Potential temperature (K), (b) decaying scalar, and (c) potential temperature (K) contours conditional on the 95th percentile of the vertical velocity for the dry convective boundary layer. In (c) the color scale is reversed (warmer air corresponds to darker shades) to increase the contrast.

However, the method is generic and the methodology can be applied to other turbulence quantities, such as variances. Similar to the analysis of Berg and Stull (2004), the JPD-based method can be applied to JPDs derived from observations.

The details of the JPD-based method are described in section 2. The large-eddy simulation (LES) data and sampling are described in section 3. In section 4 the method is applied to three convective boundary layer cases: dry convection, trade wind shallow cumulus, and stratocumulus. The shallow cumulus case is used to explore the characteristics of the JPD-based method and results are compared with traditional cloud and cloud core sampling in the cloud layer, and with the decaying tracer method of Couvreux et al. (2010). Sensitivity tests are also carried out for the shallow cumulus cases. For the dry convective case, results are compared with the decaying tracer sampling method. Summary and conclusions are presented in section 5.

2. Methodology

The methodology combines elements from similar previous studies (Wyngaard and Moeng 1992; Siebesma and Cuijpers 1995; Wang and Stevens 2000; Siebesma et al. 2007; Couvreux et al. 2010). The scalar quantity of interest is denoted by ϕ and in the present discussion corresponds to total (vapor plus cloud liquid) water mixing ratio or liquid water potential temperature, $\phi = \{q_t, \theta_l\}$.

a. Definitions

The methodology and analysis of the results is in terms of discrete variables because model data and

derived quantities are discrete. Model data are on Cartesian grids that are equispaced in the horizontal directions. The horizontal mean of a variable at model level l is

$$\overline{\phi}(l) \equiv \frac{1}{N_m} \sum_{m=1}^{N_m} \phi(l, m), \qquad (4)$$

where N_m is the horizontal sample size. For statistically stationary flows the sample size consists of horizontal planes at various time instances of an ensemble of simulations. The covariance, which approximates the turbulent flux in (1), is

$$\overline{w'\phi'}(l) \equiv \frac{1}{N_m} \sum_{m=1}^{N_m} w'(l, m)\phi'(l, m), \qquad (5)$$

where the primes denote fluctuations with respect to the mean in (4), as defined in (2). Presently, all covariances are estimated based on the resolved-scale fields and the subgrid-scale contribution is neglected. For well-resolved simulations, away from the surface, the subgrid-scale covariance part is small (<5%) (e.g., Matheou and Chung 2014).

The statistics of w and ϕ can be described by the normalized two-dimensional histogram at each vertical level; that is, $f_{w\phi}(l, i, j)$ is the relative frequency of occurrence of values in $[w(i)-\Delta w/2, w(i) + \Delta w/2] \times [\phi(j)-\Delta\phi/2, \phi(j) + \Delta\phi/2]$ at vertical level l, where the variable increments Δw and $\Delta\phi$ are presently taken as constant. Indexes (i, j) correspond to the discrete partitioning of the (w, ϕ) space. The explicit dependence on level l in the argument of the variables is dropped in the following. The term $f_{w\phi}(i, j)$ is normalized such that the

probability of occurrence of any combination of w and ϕ is unity:

$$\sum_{i=1}^{N_i} \sum_{j=1}^{N_j} f_{w\phi}(i,j)\Delta w\Delta\phi = 1. \qquad (6)$$

Essentially, $f_{w\phi}(i,j)$ is the JPD of w–ϕ. From the definition of f it follows that

$$\overline{w'\phi'} = \sum_{i=1}^{N_i} \sum_{j=1}^{N_j} w'\phi' f_{w\phi}(i,j)\Delta w\Delta\phi, \qquad (7)$$

$$g'_{w\phi}(i,j;g_0,w_0,\phi_0,\sigma_w,\sigma_\phi,r) = g_0 \exp\left[-\frac{1}{2-2r^2}\left(\frac{w''^2}{\sigma_w^2} - 2r\frac{w''\phi''}{\sigma_w\sigma_\phi} + \frac{\phi''^2}{\sigma_\phi^2}\right)\right], \qquad (8)$$

where the double prime denotes fluctuations with respect to the discrete mean of g', that is, $w(i,j) = w_0 + w''(i,j)$. The joint-Gaussian approximant has six free parameters: g_0, w_0, ϕ_0, σ_w, σ_ϕ, and r, which are the amplitude, the pairs of means and variances, and the correlation, respectively.

The present JPD approximant g' has two important differences from the joint-Gaussian fit used in Wyngaard and Moeng (1992); g' approximates f only partially, whereas in Wyngaard and Moeng (1992) the joint-Gaussian approximates the entire JPD, which constrains the means of the variables (i.e., the location of the peak). The means w_0 and ϕ_0 are free parameters in (8) and in general not equal to $\overline{w}$ and $\overline{q}$. Moreover, (8) is not a JPD, since it is not normalized [i.e., the condition in (6) is not satisfied].

The approximation g' is used to partition f into the local, $g_{w\phi}$, and nonlocal, $h_{w\phi}$, mixing contributions,

$$f_{w\phi} = g_{w\phi} + h_{w\phi}, \qquad (9)$$

where

$$g_{w\phi}(i,j) = \begin{cases} g'_{w\phi}(i,j), & \text{if} \quad g'_{w\phi}(i,j) \le f_{w\phi}(i,j) \\ f_{w\phi}(i,j) & \text{otherwise}. \end{cases} \qquad (10)$$

Equation (10) ensures that $h_{w\phi}$ is nonnegative, because, when normalized, $h_{w\phi}$ must correspond to a JPD. Equation (9) describes the essence of the JPD-based method, where the total JPD, f, is split into two parts, g and h.

b. Local mixing joint probability density function

The main novel element of the JPD-based method is to perform the decomposition of the vertical

similar to the continuous-variable definition of the covariance; N_i and N_j are the number of w and ϕ bins, respectively, of the discrete JPD.

The JPD is not known a priory and it is typically estimated from observations or model data. Presently, $f_{w\phi}$ is estimated from the frequency distribution of the w–ϕ pairs (i.e., the two-dimensional histogram) using LES model data.

A joint-Gaussian function, $g'_{w\phi}$, is introduced that partially approximates $f_{w\phi}$ (Wyngaard and Moeng 1992; Wang and Stevens 2000; Golaz et al. 2002; Larson and Golaz 2005; Bogenschutz and Krueger 2013):

turbulent flux in (3) in "JPD space" [i.e., (9) and (10)], rather than in physical space as in, for instance, Siebesma and Cuijpers (1995), Siebesma et al. (2007), and Couvreux et al. (2010). The full w–ϕ JPD is partitioned into two components corresponding to local turbulent mixing $g_{w\phi}$ and coherent motions $h_{w\phi}$. In the cumulus cloud layer the "local" mixing is often referred to as the "environment" contribution, that is, the clear air turbulent motions (Siebesma and Cuijpers 1995). In the subcloud layer and in dry convection, local mixing corresponds to turbulent motions that are not actively contributing to the updrafts or downdrafts (Couvreux et al. 2010). Conversely, the coherent motions are due to nonlocal updrafts and downdrafts.

The joint-Gaussian approximation $g'_{w\phi}$ of the local mixing should only partially approximate the full JPD $f_{w\phi}$ in a small region S_p near its peak. To determine $g'_{w\phi}$, first the region S_p in the w–ϕ-variable space is chosen and then a best fit in the form of $g'_{w\phi}$ to $f_{w\phi}$ in region S_p is sought. The iso-probability contour of value p is the boundary of the region S_p. The iso-probability contours are centered at the maximum of $f_{w\phi}$. Figures 2 and 3 show iso-probability contours centered at the JPD peak for w–q_t and w–θ_l JPDs from the shallow cumulus case. For example $S_{0.2}$ corresponds to all $(i,j) \in (p < 0.2)$. This procedure requires that all JPDs have a single maximum, which is typically the case for the JPDs of boundary layer convection.

The error, or distance, between $g'_{w\phi}$ and $f_{w\phi}$ in S_p as a function of the parameters of g' is defined as follows:
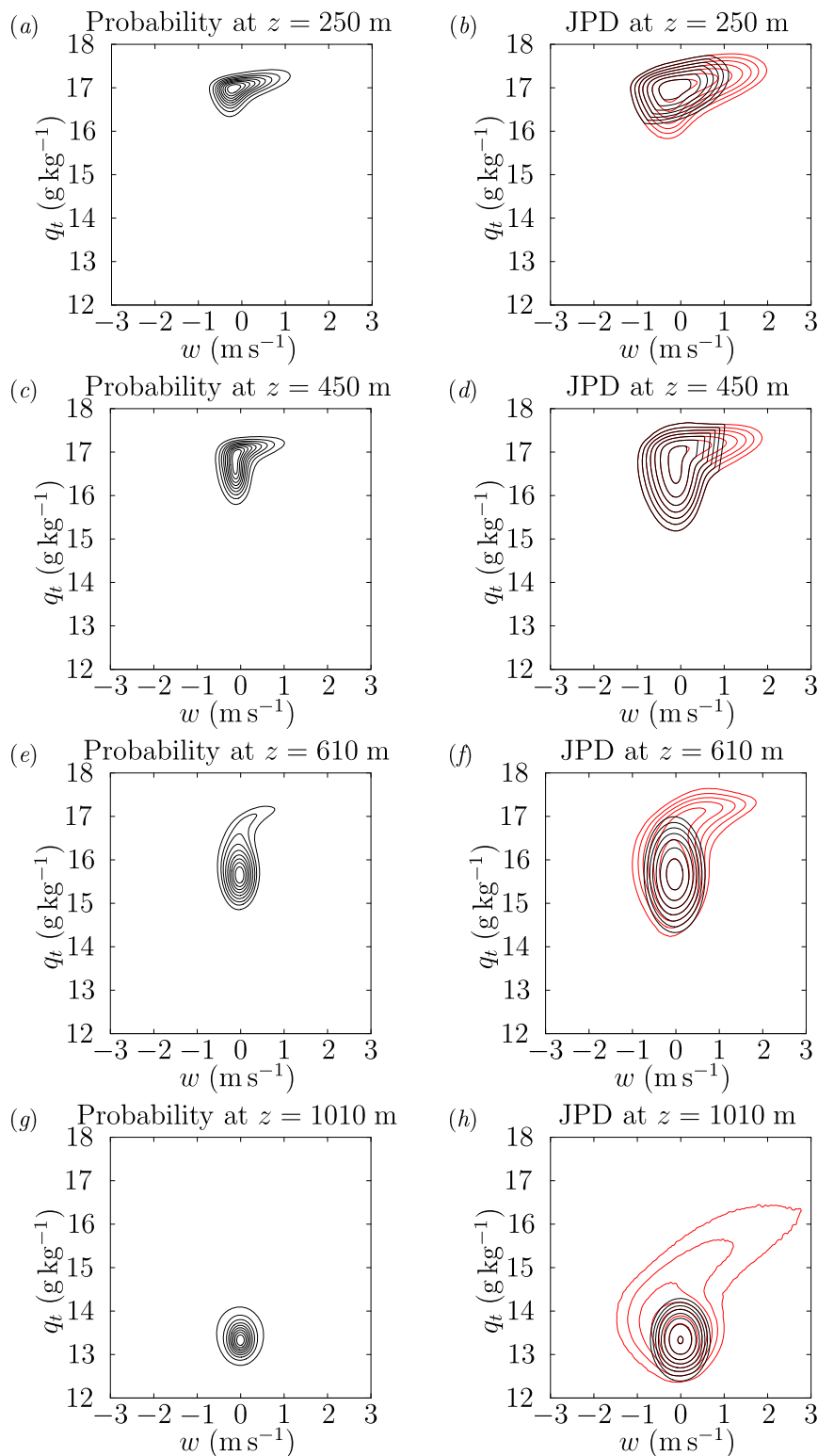
FIG. 2. Joint probability density functions (JPD) of vertical velocity w and total water mixing ratio q_t for the BOMEX shallow cumulus case at different heights. (left) Iso-probability contours at 0.1 intervals. (right) Logarithmically spaced contours of the full JPD (red) and the joint-Gaussian-based approximation (black). (a)–(d) The JPDs in the subcloud layer and (e)–(h) the JPDs in the cloud layer ($z = 510$–1600 m).
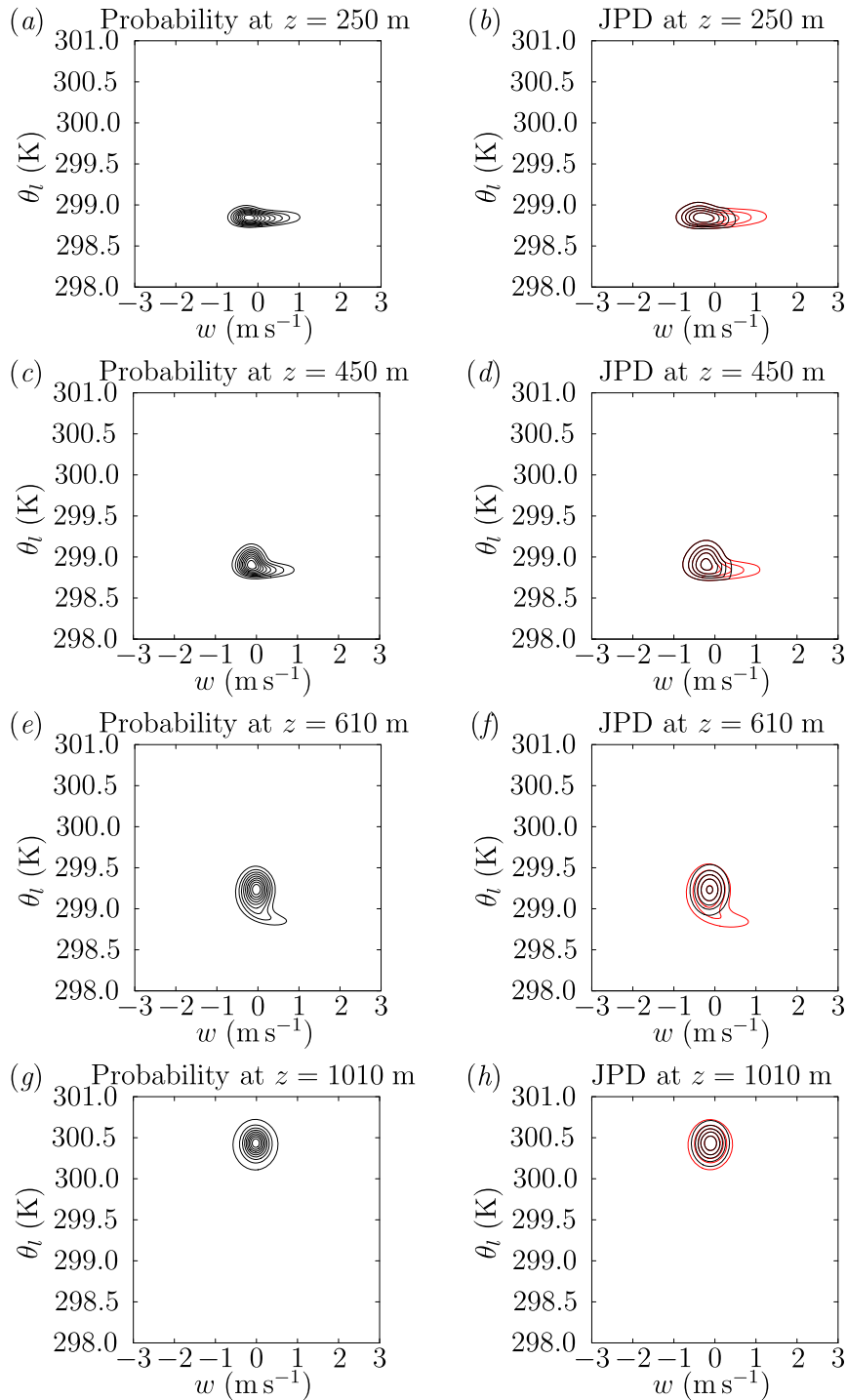
FIG. 3. Joint probability density functions (JPD) of vertical velocity w and liquid water potential temperature θ_l for the BOMEX shallow cumulus case at different heights. (left) Iso-probability contours at 0.1 intervals. (right) Logarithmically spaced contours of the full JPD (red) and the joint-Gaussian-based approximation (black). (a)–(d) The JPDs in the subcloud layer and (e)–(h) the JPDs in the cloud layer ($z = 510$–1600 m).

$$E(g_0, w_0, \phi_0, \sigma_w, \sigma_\phi, r) = \sum_{i,j \in S_p} [g\prime_{w\phi}(i,j; g_0, w_0, \phi_0, \sigma_w, \sigma_\phi, r) - f_{w\phi}(i,j)]^2. \tag{11}$$

A minimization problem is solved to determine the parameter values g_0, w_0, ϕ_0, σ_w, σ_ϕ, and r that minimize E. That is, all six parameters are determined simultaneously by finding the combination of their values that leads to the minimum of E. Even though the number of parameters is somewhat large, good initial estimates can be computed based on the statistics of $f_{w\phi}$.

The error E, and consequently $g\prime_{w\phi}$, implicitly depend on ϕ and S_p (or equivalently p). The dependence on the scalar ϕ is expected, and it is related to the flow dynamics. In contrast, $g\prime_{w\phi}$ should weakly depend on p. For large p (e.g., $p > 0.4$), $g\prime_{w\phi}$ will tend to approximate the entire $f_{w\phi}$ and thus not represent the local mixing component. For small values of p (e.g., $p < 0.05$), the procedure may not yield reliable results because the approximation becomes very local and the finescale variations of JPD can overly influence $g\prime_{w\phi}$. Here p is the only free parameter of the method and it is shown that results are not sensitive to p when $0.1 < p < 0.4$. To improve the quality of the fit, all JPDs are smoothed using the procedure described in section 2d.

c. Vertical flux decomposition

The preceding sections 2a and 2b describe the decomposition of turbulence in probability space based on the JPD of a scalar and vertical velocity. In this section the statistical quantities are linked to physical-space quantities, such as area fractions, means, and covariances.

In general, each horizontal plane can be split into N_s disjoined sets whose union is the entire plane. Thus, their area fraction α_s sum is

$$\sum_{s=1}^{N_s} \alpha_s = 1. \tag{12}$$

Similarly, if ϕ_s denotes the mean of ϕ in each subset, the total mean is

$$\overline{\phi} = \sum_{s=1}^{N_s} \alpha_s \phi_s. \tag{13}$$

The linearity of the averaging operation leads to a simple relation between the total and the sum of subset means weighted by their area fractions. In contrast, the covariance includes products of variables, and therefore its decomposition includes both the sum of weighted subset covariances and cross terms of the subset means

(e.g., Siebesma and Cuijpers 1995; Wang and Stevens 2000):

$$\overline{w\prime\phi\prime} = \sum_{s=1}^{N_s} \alpha_s (w_s - \overline{w})(\phi_s - \overline{\phi}) + \sum_{s=1}^{N_s} \alpha_s \overline{w\prime\phi\prime}^s, \tag{14}$$

where $\overline{w\prime\phi\prime}^s$ is the covariance within each subset. The notation $\phi_s \equiv \overline{\phi}^s$ is used for simplicity.

The terms included in the first term of the rhs of (14) are referred to as the "top hat" part of the turbulent fluxes (e.g., Willis and Deardorff 1974; Young 1988; Wang and Stevens 2000) because only average quantities are included (and not the within-subset correlations). The fraction of the top-hat contribution to the total covariance is denoted by

$$\beta_{\phi s} = \alpha_s (w_s - \overline{w})(\phi_s - \overline{\phi})/\overline{w\prime\phi\prime}. \tag{15}$$

Similarly, the flux fraction due to the within-subset covariance is

$$\gamma_{\phi s} = \alpha_s \overline{w\prime\phi\prime}^s/\overline{w\prime\phi\prime}. \tag{16}$$

Because in the context of turbulent flux parameterization we are interested in the relative contributions of the different terms of (14) to the total flux (e.g., Siebesma and Cuijpers 1995), results are shown in terms of the nondimensional quantities α, β, and γ. We refer to β and γ as fractions because of their definitions in (15) and (16); however, their values can be negative and/or greater than unity. Unlike, the partition of the total JPD in (9) into nonnegative functions, the component covariances of (14) can be of any sign. The only constraint on their values is due to (14):

$$\sum_{s=1}^{N_s} \beta_{\phi s} + \sum_{s=1}^{N_s} \gamma_{\phi s} = 1. \tag{17}$$

The partial JPDs $g_{w\phi}$ and $h_{w\phi}$ are used to estimate the terms in (15) and (16). On a horizontal plane the area fraction of the local mixing turbulent motions is

$$\alpha_l = \sum_{i=1}^{N_i} \sum_{j=1}^{N_j} g_{w\phi} \Delta w \Delta \phi \leq 1. \tag{18}$$

The coherent motion part of the JPD, $h_{w\phi}$, can be divided into updraft and downdraft parts based on the sign of vertical velocity:

$$h_{w\phi}^+ = h_{w\phi}|w \gtrsim 0, \tag{19}$$

$$h_{w\phi}^- = h_{w\phi}|w < 0. \tag{20}$$

Accordingly, the updraft area fraction is

$$\alpha_u = \sum_{i=1}^{N_i} \sum_{j=1}^{N_j} h_{w\phi}^+ \Delta w \Delta \phi. \tag{21}$$

Overall, $\alpha_l + \alpha_u + \alpha_d = 1$, where the subscripts l, u, and d are used to denote local mixing, updraft, and downdraft, respectively. Note that $g_{w\phi}$, $h_{w\phi}^+$, and $h_{w\phi}^-$ as defined in (10) and (19)–(20) are not proper JPDs because they do not integrate to unity. The updraft mean vertical velocity is

$$w_u = \frac{1}{\alpha_u} \sum_{i=1}^{N_i} \sum_{j=1}^{N_j} w(i,j) h_{w\phi}^+ \Delta w \Delta \phi, \tag{22}$$

and the updraft covariance is

$$\overline{w'\phi'}^u = \frac{1}{\alpha_u} \sum_{i=1}^{N_i} \sum_{j=1}^{N_j} w(i,j)\phi(i,j) h_{w\phi}^+ \Delta w \Delta \phi - w_u \phi_u. \tag{23}$$

Two decompositions are used for the vertical flux: 1) a local–coherent motion partition, $N_s = 2$ in (14), and 2) a local–updraft–downdraft, $N_s = 3$. In the latter, the updraft–downdraft part corresponds to the coherent motion part of the former. In other words, the local component is the same in the two decompositions.

d. Smoothing filter

To improve the vertical coherence of the terms in the turbulent flux decomposition, the JPDs are smoothed by applying a discrete Gaussian filter G, with width $n \times n$, where n is an odd integer. Values of $n < 10$ are presently considered. The smoothed JPD is then,

$$f_{w\phi}(i,j) = \sum_{p=-(n-1)/2}^{(n-1)/2} \sum_{q=-(n-1)/2}^{(n-1)/2} G(p,q) f_{w\phi}^*(i+p,j+q), \tag{24}$$

where $f_{w\phi}^*$ represents the JPD as estimated from the LES data. Here G is normalized such that the sum over all elements is unity. A sensitivity test to the JPD-based flux decomposition using smoothness JPD is performed in section 4a(4).

3. Large-eddy simulation

A series of large-eddy simulations is used to estimate the JPDs of vertical velocity w and liquid water potential temperature θ_l, or total water mixing ratio q_t. For the application of the JPD-based method, how the JPDs are obtained is immaterial and observations can also be used to construct the JPDs. Using LES data is advantageous because the large data size yields smooth JPDs.

The LES model of Matheou and Chung (2014) is used to simulate three shallow convection cases: shallow cumulus, dry convection, and stratocumulus. In the cumulus and dry convection cases, two decaying scalar tracers, $\phi_\alpha, \alpha = \{1, 2\}$, are included in the LES following Couvreux et al. (2010). The scalars differ in their decay time scale: $\tau_1 = 15$ and $\tau_2 = 60$ min.

The computational domain is doubly periodic in the horizontal directions. All grids are uniform and isotropic (i.e., $\Delta x = \Delta y = \Delta z$). The simulations have variable domain sizes and resolutions that adjust to the differences in boundary layer depth. A Rayleigh damping layer is used near the top of the computational domain to limit gravity wave reflection. Table 1 summarizes the LES runs.

For the dry convection and shallow cumulus cases an ensemble of LES runs is carried out. A different random initial perturbation of liquid water potential temperature and total water mixing ratio in the lowermost five vertical levels of the computational domain was used. The ensemble member number is denoted by N_{runs} in Table 1. To form all flow statistics, N_{in} instances in a time interval $t_{\text{ave}} = t_{\text{begin}} - t_{\text{end}}$ when the flow is approximately statistically stationary are used; $t = 0$ corresponds to the beginning of the LES run. That is, the size of the sample at each vertical level is $N_m = N_{\text{runs}} \times N_{\text{in}} \times N_x \times N_y$. Because of the spatial correlation of the flow fields the number of independent samples is fewer than N_m. The sampling parameters for each case are documented in Table 1.

4. Results

a. Shallow cumulus

The characteristics of the JPD-based method are mainly explored for a trade wind cumulus-topped boundary layer that was observed during the Barbados Oceanographic and Meteorological Experiment (BOMEX) campaign (Holland and Rasmusson 1973). The LES setup follows the model intercomparison study of Siebesma et al. (2003).

1) JPD-BASED DECOMPOSITION

Figure 2 shows the w–q_t JPD and Fig. 3 shows the w–θ_l JPD. JPDs at four heights are shown corresponding to half-height of the subcloud layer, cloud base, maximum of cloud fraction, and middle of the cloud layer. The left column panels of Figs. 2 and 3 show iso-probability

TABLE 1. Summary of the cases simulated. The details of the case setup are described in the references (second column). Here L_x and L_z are the horizontal and vertical domain lengths and N_x is the number of horizontal grid points. The zonal and meridional domain lengths and number of grid points are equal, and Δx is the grid spacing. For all runs the grid spacing is uniform in all directions (i.e., $\Delta x = \Delta y = \Delta z$). The term N_z is the number of vertical model levels, N_{runs} is the size of the simulation ensemble, t_{ave} is the time interval used for data sampling to construct the JPDs, N_{in} is the number of instances used in t_{ave}, and N_m is the number of the data sample used to estimate the JPD.

Case	Reference	L_x (km)	L_z (km)	Δx (m)	N_x	N_z	N_{runs}	t_{ave} (h)	N_{in}	$N_m \times 10^6$
Dry convection	Siebesma et al. (2007), case 3	10.24	2	10	1024	200	4	6	1	4.2
Shallow cumulus	Siebesma et al. (2003)	20.48	3	20	1024	150	8	4–6	5	42
Stratocumulus	Stevens et al. (2005)	5.12	1.5	1.25	4096	1200	1	1.5–2	16	268

contours centered on the JPD maximum. The right column panels show logarithmically spaced contours of the full JPD in red color and the joint-Gaussian-based approximation in black. Only 0.3 of the probability fraction [i.e., $p = 0.3$ (section 2b)] was used in fitting the joint-Gaussian g' JPD. Sensitivity of the results with respect to p and the JPD smoothness is discussed in section 4a(4). The joint Gaussian well approximates the peak of the JPD in the cloud layer, where also $g' < f$. In the subcloud layer, constraint (10) is applied because the JPDs are "steeper" than the joint Gaussian in some regions resulting in overlap of the g and f contours in Figs. 3b and

3d. The g contours appear as nearly straight lines where g' is not constrained. This does not necessarily invalidate the assumption of the local mixing component represented by a joint-Gaussian JPD. It can be interpreted as a modification of the local mixing by the large-scale (coherent) convective motions.

Figure 4 shows the vertical flux decomposition for q_t (top row) and θ_l (bottom row). Two decompositions are used: coherent–local and updraft–downdraft–local partitions. The fractional contributions are denoted by β_ϕ for the top-hat part and γ_ϕ for the within-subset covariance. For the coherent–local $\overline{w'q_t'}$ partition
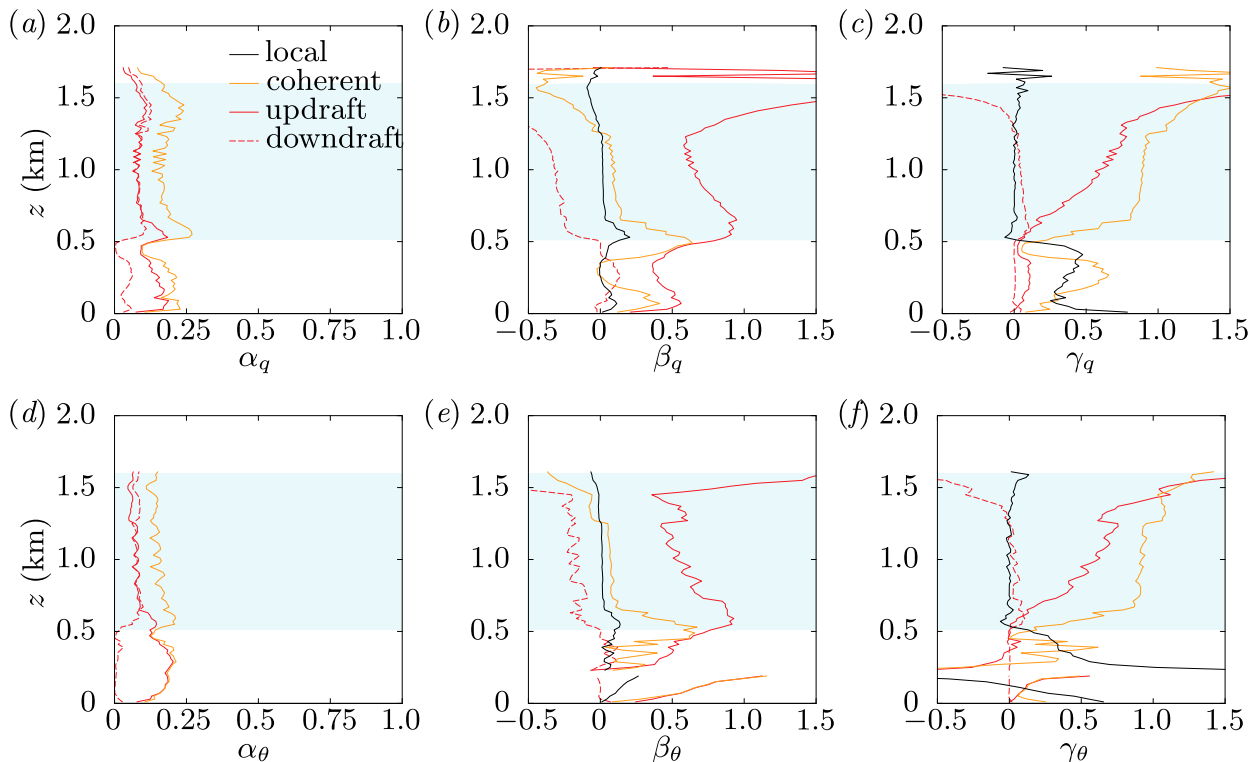

FIG. 4. (top) Vertical flux decomposition for total water mixing ratio and (bottom) liquid water potential temperature for the BOMEX shallow cumulus case using the JPD-based method. (a),(d) The area fraction α; (b),(e) the top-hat fraction of the flux β; and (c),(f) the within-subset covariance fraction γ. Two decompositions are used: a local mixing–coherent structures partition and local mixing–updraft–downdraft. The shaded area corresponds to the cloud layer.

$\beta_{qc} + \beta_{ql} + \gamma_{qc} + \gamma_{ql} = 1$, and for the updraft–downdraft–local partition $\beta_{qu} + \beta_{qd} + \beta_{ql} + \gamma_{qu} + \gamma_{qd} + \gamma_{ql} = 1$. Here β_θ and γ_θ are discontinuous when $\overline{w'\theta_l'}$ is zero at $z \approx 200$ m. The shaded area corresponds to the cloud layer that for BOMEX is located between 0.51 and 1.60 km. Note that although the liquid water mixing ratio q_l is nonzero above 1.60 km because of cloud penetration into the inversion layer, the turbulent fluxes are zero.

The area fractions of the updraft and downdraft (and their sum: the coherent part of the flow) exhibit small dependence on the thermodynamic variable. The differences are larger in the subcloud layer and quantitatively reflect the differences in the JPDs. For instance, $\alpha_{\theta d}$ (the downdraft area fraction based on θ_l) in the subcloud layer is negligible, whereas $\alpha_{qd} \approx 0.05$, which correspond to the presence (in the w–q_t JPD) and absence (w–θ_l JPD) of tails with negative vertical velocities (Couvreux et al. 2007). For the q_t statistics at the cloud base ($z = 450$ m in Fig. 2), as the major axis of the double-Gaussian transitions toward the vertical direction in the w–q_t coordinates of the figure, the negative w part of the JPD tail diminishes and the downdraft area fraction is zero (Fig. 4a). The updrafts account for nearly the entire area fraction of the coherent motions in the subcloud layer, whereas in the cloud layer updrafts and downdrafts contribute equally to the coherent motion area fraction.

In the coherent–local decomposition the top-hat fractions, β_{qc} and $\beta_{\theta c}$ (orange solid lines), are significant only in a layer centered at the cloud base with thickness ~300 m and near the surface. In the cloud layer, at $z > 700$ m (higher than the maximum cloud fraction), the within-region covariance is the dominant contribution to the total flux, with γ_{qc} and $\gamma_{\theta c} > 0.8$. In the subcloud layer, the local and coherent within-region covariances contribute approximately equally to the total flux. Perhaps as expected for the BOMEX case, γ_{ql} and $\gamma_{\theta l}$ (black lines) are negligible in the cloud layer since no vertical transport occurs in the clear air.

The flux contribution characteristics change when the updraft–downdraft–local decomposition is considered. The classical (Siebesma and Cuijpers 1995) character of convection emerges with the updraft terms being the primary contributors to the vertical flux in the cloud layer. The fractional flux contributions are similar for q_t and θ_l. The largest difference between the two variables is the magnitude of the top-hat fraction for updraft and downdraft in the cloud layer where $\beta_{\theta u}$ and $\beta_{\theta d}$ are somewhat smaller in absolute value than the corresponding β_{qu} and β_{qd}. The terms β_{qd} and $\beta_{\theta d}$ are significant in the cloud layer and, as expected, have the opposite sign of the total flux. In the subcloud layer, the flux decomposition is similar to the coherent–local

partition (i.e., $\beta_d \approx 0$ and $\gamma_d \approx 0$, and β_u and γ_l contribute approximately equally to the total flux).

The vertical fluxes decomposition is similar for q_t and θ_l, with the largest differences in the subcloud layer. Marked variations with respect to height in the contributions to the total flux are observed near cloud base.

Unlike other conditional sampling methods, the JPD-based method is applied independently for each thermodynamic variable. Thus, in general the area coverage of the flow regions can differ based on the JPD variable. Area fractions and vertical flux components exhibit finescale wiggles, which are often observed in similar flow statistics (e.g., Romps 2010), because minimization in (11) is performed independently at each level. In other words, g' is not directly linked to a vertical transport equation, as in the case of the decaying scalar sampling that results in profiles with strong vertical coherence. The wiggles are not a result of poor sampling as discussed in the method sensitivity section [section 4 a(4)].

2) DECAYING SCALAR DECOMPOSITION

The results of the JPD-based method are compared with two commonly used conditional sampling techniques: the method of Couvreux et al. (2010) and the classical cloud and cloud core (Siebesma and Cuijpers 1995) decomposition (discussed in the next section). The conditional sampling based on a decaying scalar is somewhat ambiguous with respect to the variance threshold and the scalar decay time scale τ. The values of $m = 2.5$ for the variance threshold factor and $\tau = 15$ min for the scalar decay time scale are used for the BOMEX case. The rationale for these choices and further details are discussed in the appendix.

Figure 5 shows the vertical flux decomposition of $\phi = \{q_t, \theta_l\}$ for the BOMEX shallow cumulus case using the conditional sampling method (top and bottom rows, respectively). The partition is designated as updraft–local, even though the term local is somewhat misleading because it includes the contributions from downdrafts. It is used to denote the complement of the updraft subset, rather than strictly local mixing. Because an additional variable is used to sample the flow, the area fraction of the updraft structures is independent of the thermodynamic variable, thus only one area fraction panel is shown (Fig. 5a).

The updraft top-hat flux fractions, β_{qu} and $\beta_{\theta u}$, are qualitatively similar to those of the JPD-based method; β_{qu} is in better agreement with the corresponding fraction estimated using the JPD-based method than $\beta_{\theta u}$. The better agreement of β_{qu} may be because cloud liquid, which is strongly related to q_t, is used for the updraft selection in the conditional sampling method. The conditional sampling method results in vertically coherent
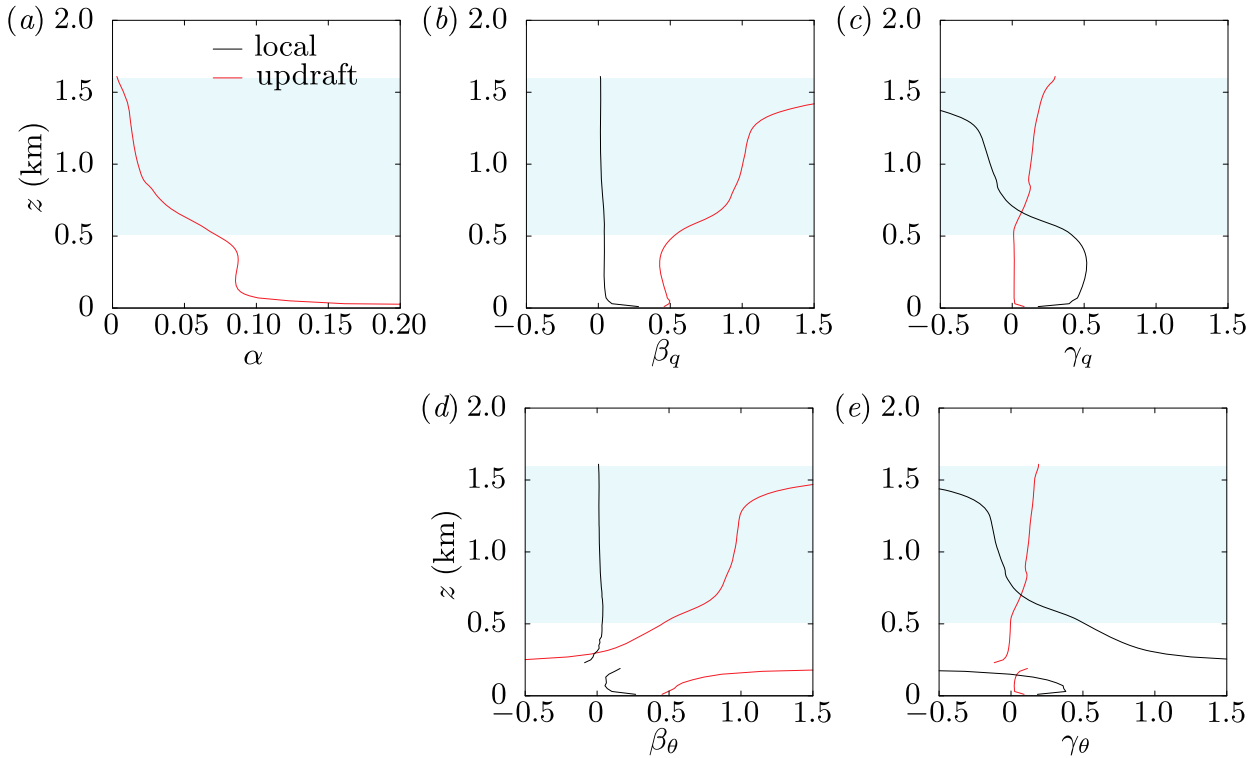
FIG. 5. (top) Vertical flux decomposition for total water mixing ratio and (bottom) liquid water potential temperature for the BOMEX shallow cumulus case using the conditional sampling method of Couvreux et al. (2010). (b),(d) The top-hat fraction of the flux β; and (c),(e) the within-subset covariance fraction γ. The area fraction of the coherent structures is independent of the thermodynamic variable and is only shown in (a). The shaded area corresponds to the cloud layer.

(smooth) curves because it is based on the decaying scalar variance, which smoothly varies in the vertical.

In the cloud layer, β_u accounts for nearly the entire flux. This is because of a perhaps fortuitous cancelation of γ_u and γ_l in the BOMEX case (Figs. 5c and 5e). It is not clear if this cancelation is a universal character of cumulus convection or specific to the present case.

3) CLOUD DECOMPOSITION

Figure 6 shows the vertical flux decomposition based on the cloud and cloud core sampling. Cloudy grid cells are those with liquid water mixing ratio $q_l > 1 \times 10^{-5}\,\text{kg kg}^{-1}$. Cloud core is defined as cloudy grid cells with positive vertical velocity and buoyancy; that is, $q_l > 1 \times 10^{-5}\,\text{kg kg}^{-1}$, $w > 0$, and $\theta_v > \langle \theta_v \rangle$, where the angle brackets denote the instantaneous horizontal average. As in the conditional sampling decomposition, the complement of the cloud/cloud core is designated as the local component of mixing that also includes the downdrafts contribution. The cloud and cloud core decompositions are common but are reproduced here using the same dataset (Table 1) as the other runs for completeness.

The cloud and cloud core decomposition results are similar to those of the JPD-based method and the

conditional sampling using a decaying scalar. The most important difference is that the updraft top-hat term in the cloud and cloud core decompositions does not vary considerably with respect to height whereas both JPD-based and the conditional sampling methods show small variation in the cloud layer and larger variations near cloud base.

The present results corroborate previous arguments (e.g., Couvreux et al. 2010) that considering only the cloud–clear decomposition in the cloud layer of cumulus convection obscures the full character of flow. The JPD-based and the conditional sampling methods show strong differences between the subcloud and cloud layers. Moreover, the present results show that the complement of the cloudy updrafts is not the large-scale environment, as put forth in Siebesma and Cuijpers (1995), and that the negative top-hat contribution of the downdraft can cancel the within-updraft covariance.

4) SENSITIVITY TO PROBABILITY FRACTION AND JPD SMOOTHNESS

The sensitivity of the JPD-based flux decomposition is explored with respect to the probability fraction, p, which is the main parameter of the method, the sample
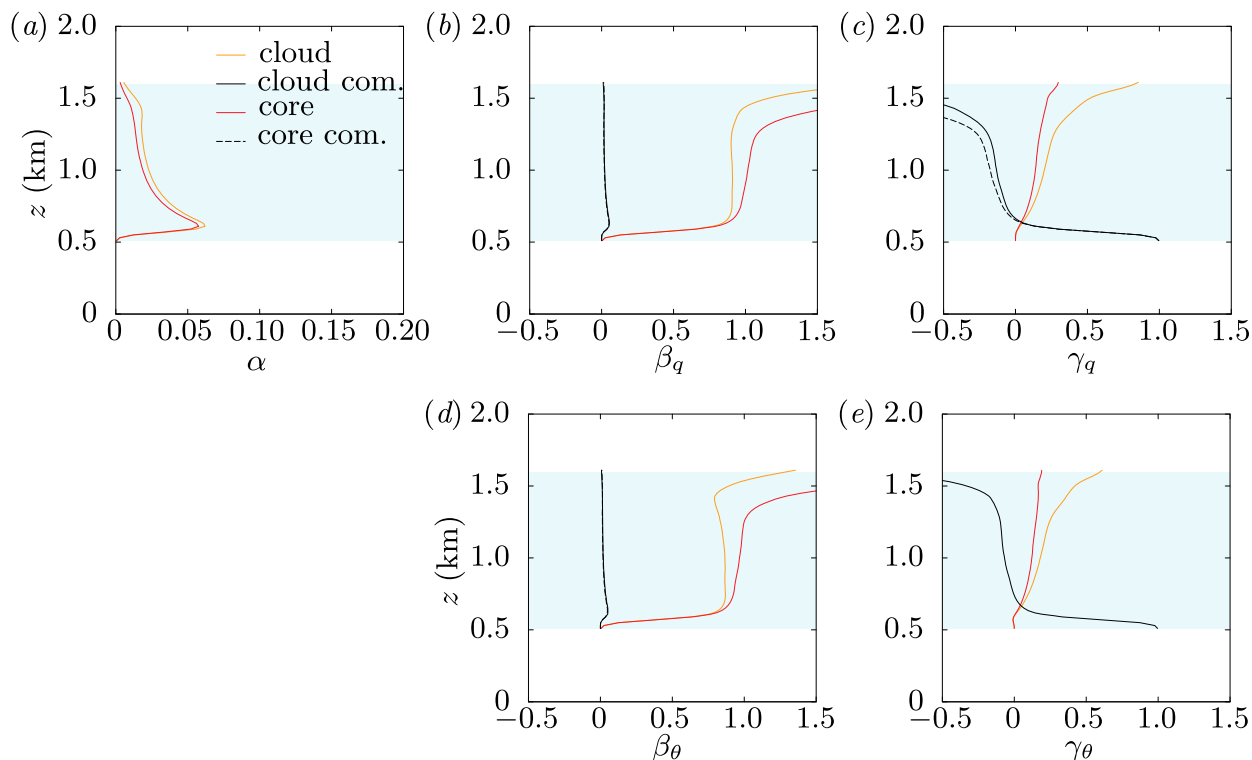
FIG. 6. (top) Vertical flux decomposition for total water mixing ratio and (bottom) liquid water potential temperature for the BOMEX shallow cumulus case based on the cloud–clear partition. (b),(d) The top-hat fraction of the flux β; and (c),(e) the within-subset covariance fraction γ. The area fraction of the coherent structures is shown in (a). The black lines correspond to the complement of the cloud and cloud core decompositions. The shaded area corresponds to the cloud layer.

size, and the smoothness of the JPD. For sufficiently converged JPDs with respect to the sample size (i.e., the "shape" of the JPD does not change when the sample size is increased), the JPD smoothness and sample size are related parameters, since larger samples should yield smoother JPDs. The BOMEX shallow cumulus case is used for all the sensitivity tests. The updraft properties are compared in all sensitivity tests because these are the most important quantities for convection parameterizations. The other statistics exhibit similar behavior.

Figure 7 shows sensitivity of the updraft area fraction α_u, top-hat fraction β_u, and within-region covariance fraction γ_u, with respect to p. Five values of p in $[0.1, 0.5]$ are used. The results for the decompositions of $\overline{w'q'_l}$ and $\overline{w'\theta'_l}$ are similar. The vertical coherence/smoothness of the area and flux fractions is reduced for small probability fractions $p < 0.3$, because the fit is performed over a small subset of the JPD and it is more susceptible to the small variations in the shape of the JPD between different vertical levels. The largest differences with respect to p are in the area fractions in the subcloud layer. This is likely because in this region the JPD shape near the peak somewhat deviates from a joint Gaussian

(Figs. 2 and 3). In spite of the small dependence of α in the subcloud layer, the flux fractions, which are the most important for convection parameterizations, are not sensitive to p.

The overall insensitivity of the results with respect to p is a confirmation that the shape of the JPDs near the peak is nearly joint Gaussian. The value of $p = 0.3$ is used, which is a compromise between smooth area and flux fractions and the requirement that the joint Gaussian only approximates the peak of the JPD.

The sensitivity with respect to the sample size is shown in Fig. 8. Decompositions are computed using a single LES run and ensembles with two, four, and eight members. From each run, five model outputs are used. The outputs are separated by equal time intervals in 4–6 h, when the flow is in quasi-stationary state. The results do not depend on the ensemble size and a single LES run is sufficient to capture the JPDs, especially for the flux fractions of q_t.

The effect of the smoothing filter width is shown in Fig. 9 for $n = 1, 3, 5, 7$, and 9, where $n = 1$ denotes no smoothing filter. A single run is used to construct the JPDs. Applying a smoothing filter improves the vertical
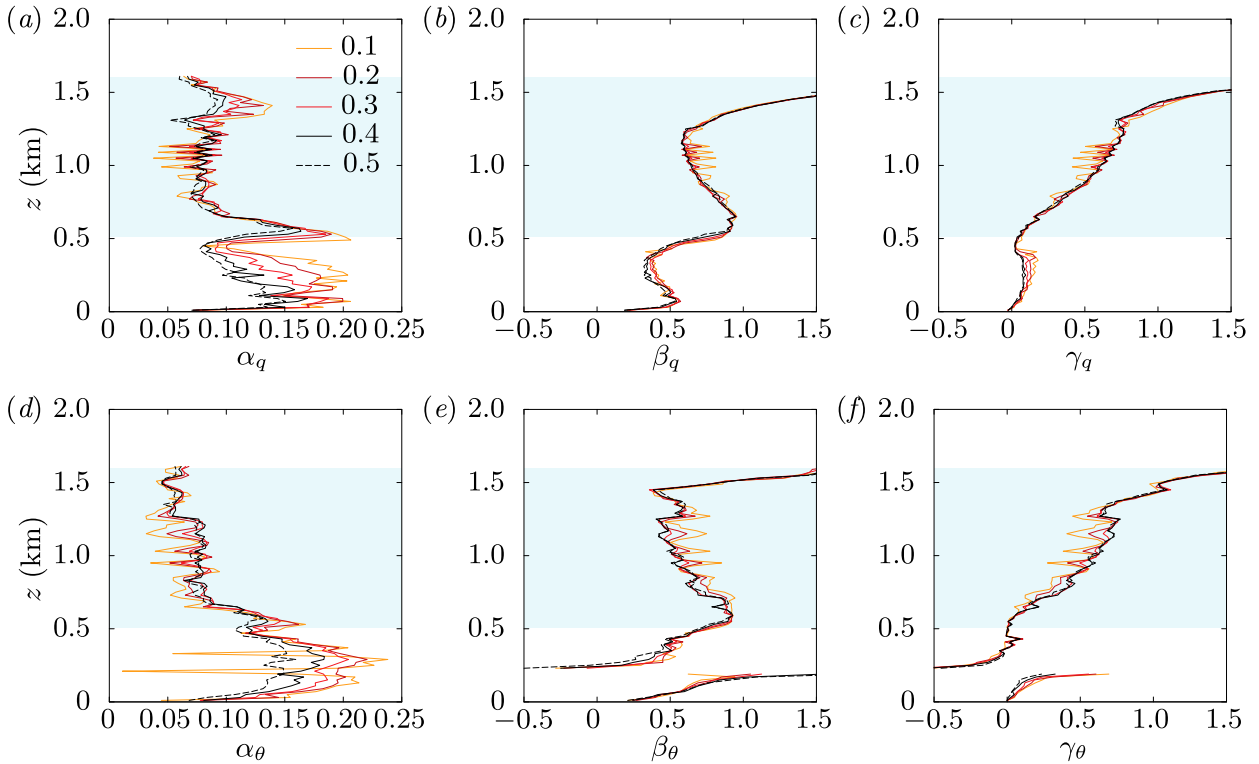
FIG. 7. Sensitivity of the JPD-based method to the probability fraction used for fitting the joint-Gaussian JPD. The panels show the BOMEX shallow cumulus case updraft quantities: (a),(d) area fraction; (b),(e) top-hat contribution; and (c),(f) within-updraft covariance. (top) The JPD-based method applied to total water mixing ratio and (bottom) liquid water potential temperature. The shaded area corresponds to the cloud layer and the legend to the probability fraction.

coherence of the decomposition statistics. The flux decomposition results show no dependence on the width of the filter. The area fractions show only minor dependence for $n \geq 3$. This implies that the overall shape of the JPD is accurately captured using a single LES run and that smoothing can be used to reduce some JPD convergence errors.

Overall, the decomposition is not sensitive to sample size and smoothness of the JPD. However, the vertical coherence can be improved when a smoother JPD is used. Moreover, the application of a smoothing filter does not alter the results and only improves the vertical coherence.

b. Dry convection

The flux decomposition is computed for the dry convective case 03 of Siebesma et al. (2007). The JPD-based method and the conditional sampling using a decaying scalar are used. Figure 1 shows a vertical plane of the potential temperature field (top panel) and a decaying scalar (middle panel). Unlike the BOMEX case, in which the forcing is well balanced and a quasi-stationary state is attained following the initial transient, the

boundary layer in the dry convective case constantly evolves. To avoid the influence of the evolving mean on the JPDs, only one time instance is used at $t = 6$ h, when the depth of the boundary layer is about 1 km. Four statistically identical LES runs are used to construct the JPDs of w–θ (water vapor is not included in the dry convection simulations). Further details about the evolution of the boundary layer, the mean fields, and updraft sampling based on the vertical velocity are discussed in Siebesma et al. (2007).

Figure 10 shows JPDs of vertical velocity w and potential temperature θ at four heights. Similar to the JPDs in the subcloud layer of the BOMEX case (Fig. 3), the peak of the JPD is offset with respect to the mean, especially for w. This results in substantial contributions from the top-hat part of the fluxes corresponding to the local component $\beta_{\theta l}$. As shown in Fig. 11, $\beta_{\theta l} \approx 0.25$ up to the height where $\overline{w'\theta'}$ switches sign.

The updraft area fraction is about 0.4 up to half the boundary layer height and decreases higher up to about 0.25. The downdraft area fraction is maximum near the boundary layer top corresponding to the entrainment process and also relatively large (fraction of about 0.1)
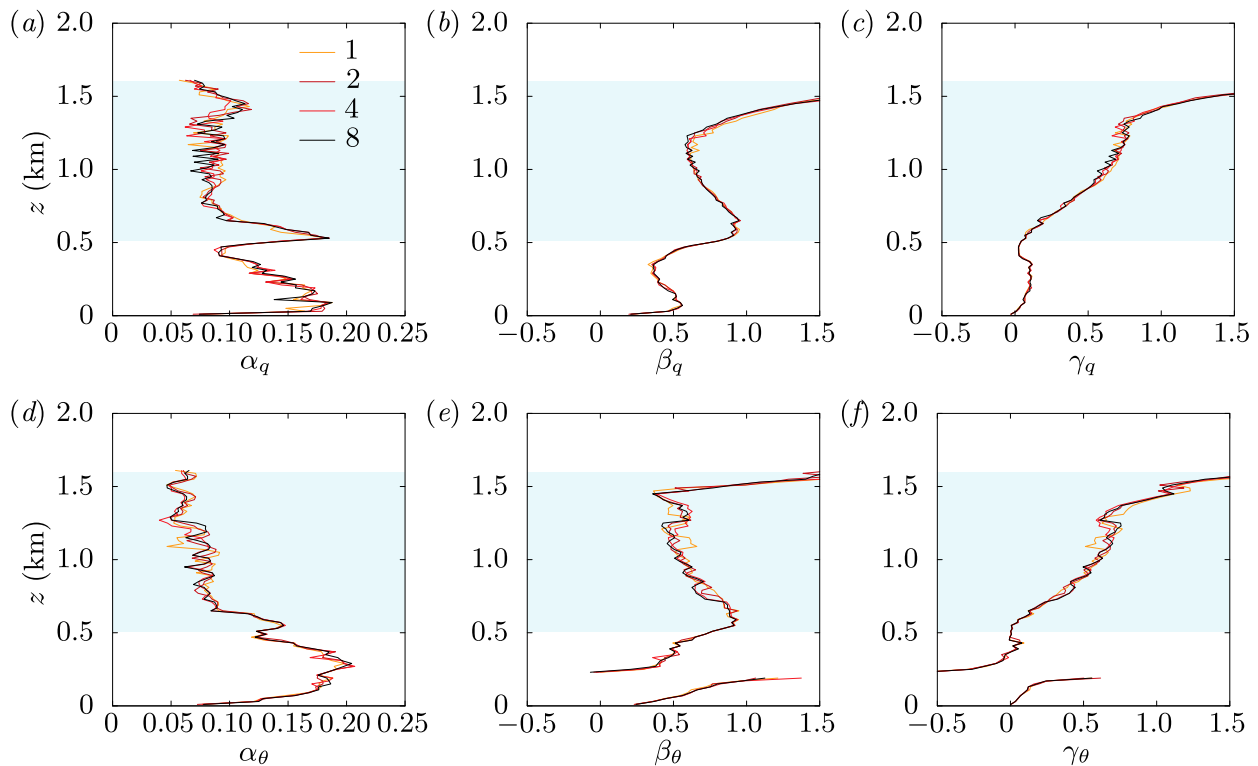
FIG. 8. Sensitivity of the JPD-based method to the run ensemble size. The BOMEX shallow cumulus case updraft quantities: (a),(d) area fraction; (b),(e) top-hat contribution; and (c),(f) within-updraft covariance. (top) The JPD-based method applied to total water mixing ratio and (bottom) liquid water potential temperature. The shaded area corresponds to the cloud layer and the legend to the ensemble size.

near the surface with a minimum value at about $z = 700$ m. The reduction of the downdraft area fraction corresponds to the change of the location of the tail of the JPD. As shown in Fig. 10, at $z = 250$ m the tail includes negative w values, but the fraction of $w < 0$ in the JPD tail is negligible at $z = 500$ and 750 m. Near the boundary layer top, $z = 900$ m, the JPD has two tails extending to positive and negative w.

In the coherent–local decomposition, $\beta_{\theta c}$ is the largest contribution except for $z < 250$ m where $\gamma_{\theta c}$ is the largest one; $\gamma_{\theta l}$ is negligible throughout the boundary layer. In the lower quarter of the boundary layer $\beta_{\theta c} \approx \beta_{\theta l}$.

In the updraft–downdraft–local decomposition, the largest contribution to the flux is from $\beta_{\theta u}$ accounting for about half of $\overline{w'\theta'}$. The remaining half of the flux is about equally split between $\beta_{\theta l}$ and $\gamma_{\theta u}$. This balance is altered at the top of the boundary layer ($\overline{w'\theta'} < 0$), where the downdraft top-hat term $\beta_{\theta d}$ becomes important and $\beta_{\theta l}$ is small.

Figure 12 shows decomposition using the conditional sampling method based on a decaying scalar. Without the presence of cloud to guide the choice of the method parameters the ad hoc choice of $\tau = 15$ m and $m = 1$, for the scalar decay time scale and variance factor threshold

was made, similar to Couvreux et al. (2010). Further details regarding the dependence of the results on τ and m are discussed in the appendix. The decaying scalar decomposition has the property of selecting the largest values of θ and w, thus the magnitude of the flux components β_θ and γ_θ is very large. The balance is between the positive (i.e., same sign as $\overline{w'\theta'}$) contribution of $\beta_{\theta u}$ and the negative $\gamma_{\theta l}$. For the chosen τ and m, the two terms, $\beta_{\theta u}$ and $\gamma_{\theta l}$, are approximately equal.

c. Stratocumulus

The stratocumulus-topped boundary layer shares many of the difficulties of dry convection with respect to updraft/downdraft conditional sampling because of the absence of convective cloud. The JPD-based method is applied to an LES of the DYCOMS II RF01 case (Stevens et al. 2005)—a nocturnal stratocumulus cloud with 100% cloud cover. The LES has very high resolution, $\Delta x = 1.25$ m, to resolve the entrainment process below the sharp inversion. Such high vertical resolution is not needed for the flux decomposition in the boundary layer, thus the JPDs are constructed by sampling four LES-model levels to create JPDs every 5 m. The present run (Matheou et al. 2017) is a higher-resolution
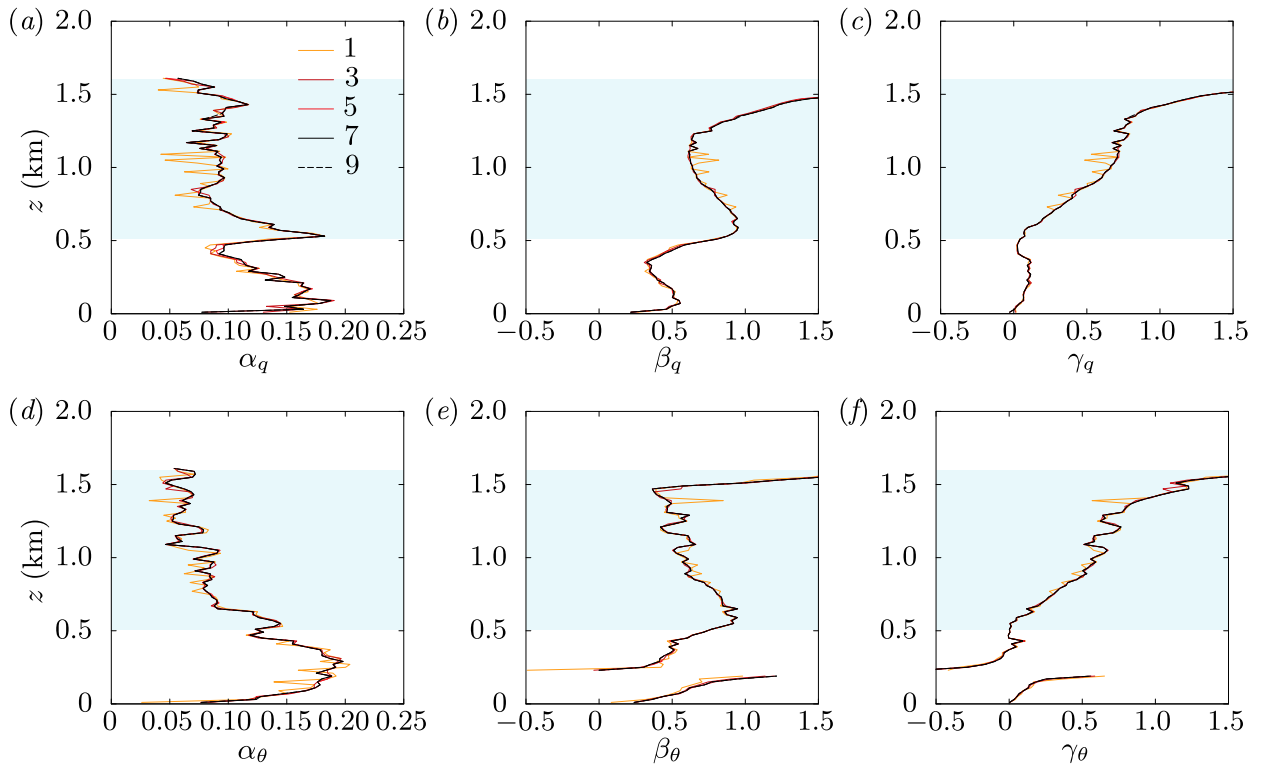
FIG. 9. Sensitivity of the JPD-based method to the smoothing filter width. The BOMEX shallow cumulus case updraft quantities: (a),(d) area fraction; (b),(e) top-hat contribution; and (c),(f) within-updraft covariance. (top) The JPD-based method applied to total water mixing ratio and (bottom) liquid water potential temperature. The JPDs were estimated from five instants of a single LES run in $t = 4$–6 h. Decompositions for four discreet Gaussian filters widths with sizes $n \times n$ and a case without any smoothing filter $n = 1$ are compared. The shaded area corresponds to the cloud layer and the legend to the filter width.

complement of the series of DYCOMS II RF01 runs in Matheou and Chung (2014), where more details about the boundary layer structure are documented.

Figure 13 shows w–q_t JPDs and Fig. 14 the w–θ_l JPDs at three vertical levels together with the joint-Gaussian based fits. The JPDs are similar to those of the dry convection case with two tails extending to positive and negative w. The long positive w tails observed in the cloud layer of the cumulus case are not present in the stratocumulus cloud layer ($z = 750$ m). The negative w tail of the JPDs is more prominent compared to the dry and cumulus convection cases because of the downdrafts generated by cloud-top radiative cooling.

Figure 15 shows the flux decomposition for the DYCOMS case. Unlike the cumulus convection case, only the area fractions for the q_t and θ_l decompositions are similar. The flux decompositions for $\overline{w'q_t'}$ and $\overline{w'\theta_l'}$ show large differences in the contribution of the various terms, especially in the cloud layer.

The coherent motions area fraction α_c varies between 0.10 and 0.25 throughout the boundary layer with the maximum area fraction near the surface and the

boundary layer top. Near the surface the updrafts account for essentially all the coherent part of the flow whereas near the boundary layer top the downdrafts account for most of the coherent motions. The flux decomposition shows complex variability with respect to height. Near the boundary layer top, β_d accounts for almost the entire vertical flux. In the subcloud layer the dominant contributions to the flux are from $\underline{\beta_u}$ and γ_l. At cloud base, $z \approx 500$ m, the decomposition of $\overline{w'\theta_l'}$ exhibits large adjustments between the different terms and includes a region ($z = 600$–720 m) where $\gamma_{\theta l}$ accounts for the entire flux.

5. Conclusions

A method based on the joint probability density function (JPD) of vertical velocity and a scalar, such as the total water mixing ratio or potential temperature, is developed to characterize coherent motions (i.e., up-drafts and downdrafts) in the atmospheric boundary layer. The JPD-based method partitions the full JPD into a joint-Gaussian part and the complement to
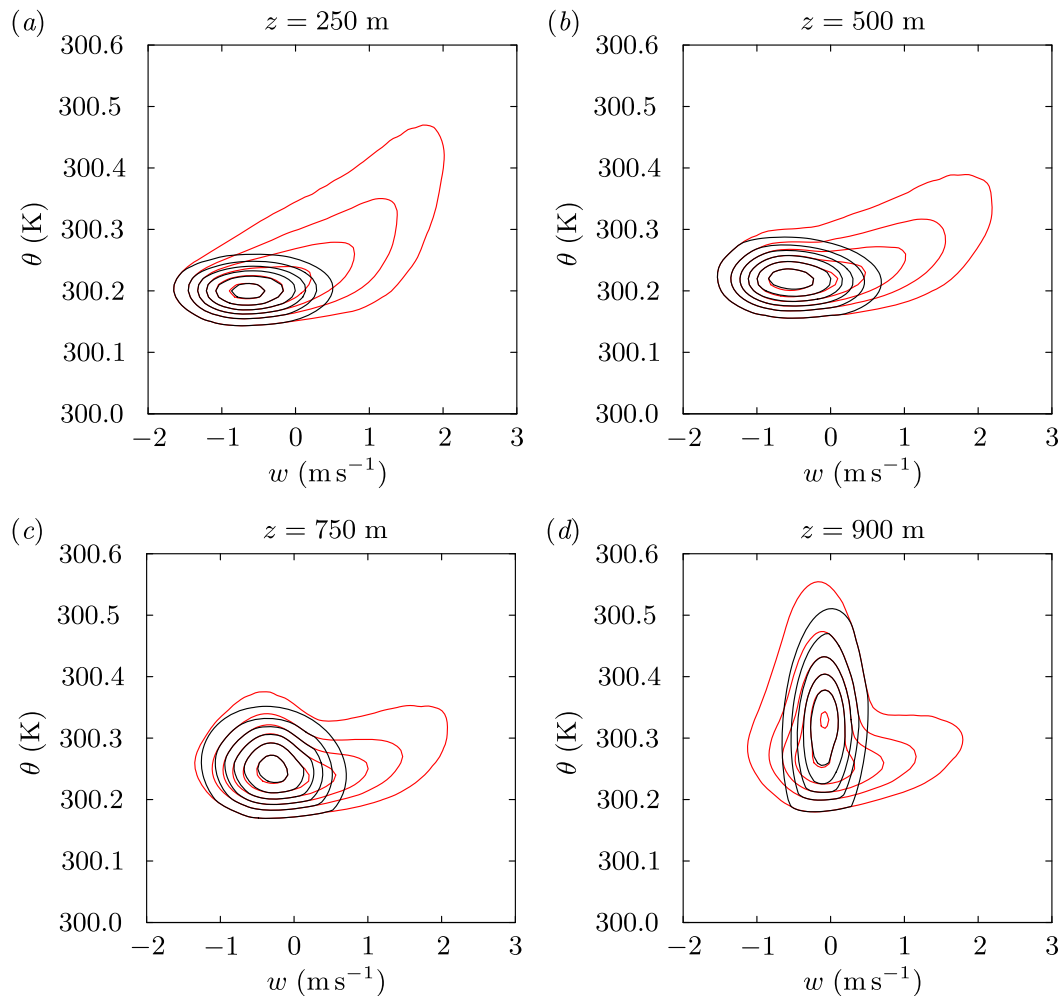
FIG. 10. Joint probability density functions (JPD) of vertical velocity w and potential temperature θ for the dry convection case at different heights. Red contours correspond to the full JPD and black contours at identical intervals to the joint-Gaussian-based approximation. The contour spacing is logarithmic.

separate the local mixing and coherent motion contributions to the JPD and, consequently, to the vertical turbulent flux. Two flux decompositions are explored: a local–coherent and a local–updraft–downdraft partition, where the local mixing fraction of the flow is the same in the two decompositions. The overarching goal of the method is to guide the development and evaluation of boundary layer convection parameterizations.

The flow decomposition is performed independently for each scalar variable. Thus, it is specific to the corresponding turbulent flux (e.g., $\overline{w'q_t'}$ or $\overline{w'\theta_l'}$). The joint Gaussian is determined by finding the best fit to the full JPD in an area near the JPD peak. This is motivated by the observation that the JPD peak has approximately joint-Gaussian shape. The present results support this proposition.

The main difference of the present method with respect to other conditional sampling methods is the decomposition of the flow in probability space rather than physical space. The JPD-based method relies on a direct identification and partition of the physical processes by considering the properties of the JPD, rather than a conditional assignment of flow regions (e.g., grid cells) to a specific category or flow subset.

The main advantages of the JPD-based method are the following:

• The flow decomposition does not depend on water condensate (cloud) and can be applied to cloud-free convection, the subcloud layer of cumulus convection, and in regions of stratiform cloud.

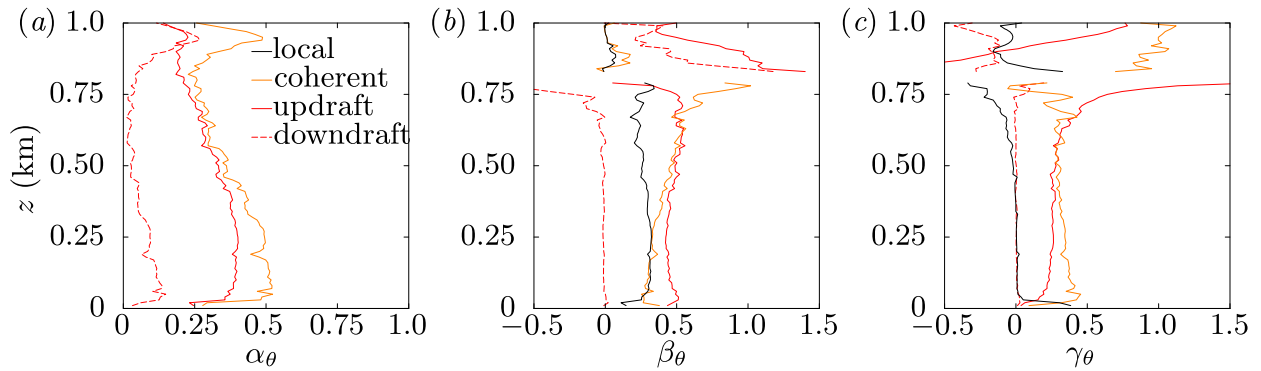• The only requirement for the application of the method is an accurate JPD. The JPD-based method

FIG. 11. Vertical flux decomposition for potential temperature for the dry convection case using the JPD-based method: (a) area fraction α; (b) top-hat fraction of the flux β; and (c) within-subset covariance fraction γ. Two decompositions are used: a local mixing–coherent structures partition and local mixing–updraft–downdraft.

does not use additional variables, such as tracers. Only the two variables forming the covariance are used. Accordingly, the method can be applied to both observational and model data.

- The covariance decomposition is specific to the scalar variable (e.g., humidity or temperature), and subtle differences between thermodynamic variables can be discerned.
- The JPD-based method includes only one free parameter and sensitivity tests show weak dependence on the parameter values.

The main disadvantage of the JPD-based method is the weak vertical coherence of the area and flux fraction profiles. That is, often the profiles are not smooth and feature "spikes." This limitation can be mitigated with additional smoothing of the JPD or the flux profiles.

The JPD-based method is applied to large-eddy simulation (LES) model output of three boundary layers: dry (cloud free) convection, the BOMEX cumulus convection case, and the DYCOMS II RF01 stratocumulus case. The results of the JPD-based method are

compared with traditional cloud and cloud core conditional samplings for the cumulus case and the decaying scalar conditional sampling method of Couvreux et al. (2010) for the dry and cumulus convection cases.

In conditional sampling methods based on flow variables (e.g., cloud) the subgrid-scale (SGS) contribution to the fluxes, when available, can be readily included in the flux decomposition by adding the SGS contribution to the resolved-scale counterpart in each grid cell. The inclusion of the SGS contribution to the JPD is not straightforward because a model for the SGS JPD is required to construct the total (resolved scale + SGS) JPD, similar to Matheou et al. (2010). Typically, the SGS contribution to the fluxes is very small (<5%) away from the surface and the flux decomposition based only on the resolved scale fields is representative of the flow.

Overall, the results of the JPD-based method are similar to the cloud and decaying scalar conditional sampling methods. However, in spite of the similarities between the different methods, important differences are observed in the three boundary layer types presently
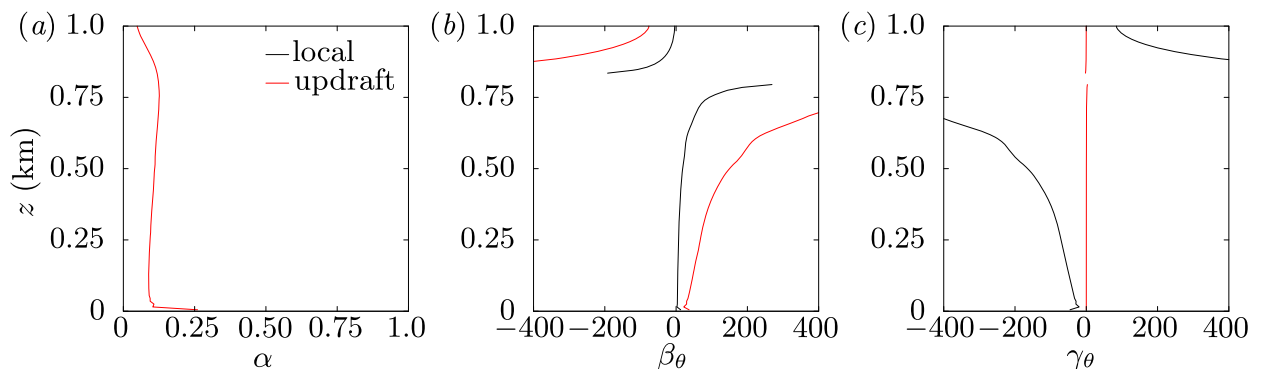

FIG. 12. Vertical flux decomposition for potential temperature for the dry convection case using the conditional sampling method: (a) area fraction α; (b) top-hat fraction of the flux β; and (c) within-subset covariance fraction γ.
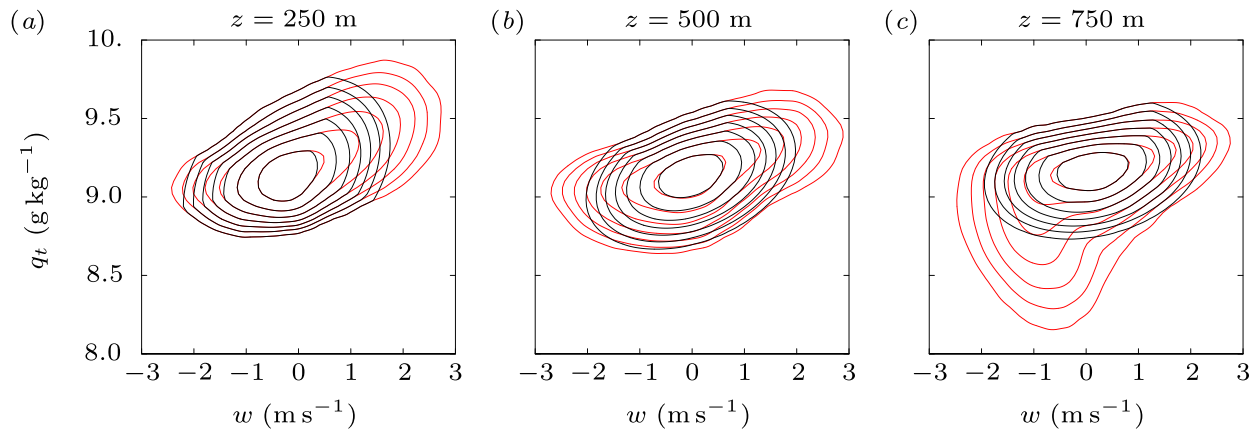
FIG. 13. Joint probability density functions (JPD) of vertical velocity w and total water mixing ratio q_t for the DYCOMS II RF01 stratocumulus case at three heights. Red contours correspond to the full JPD and black contours at identical intervals to the joint-Gaussian-based approximation. The contours are logarithmically spaced.

explored. The differences show that an objective definition of the various flow regions is elusive and that flow properties, such as updraft characteristics, depend on the sampling method. For instance, in the BOMEX shallow cumulus case the cloud and cloud core conditional samplings show that the updraft top-hat term accounts for the entire vertical flux in the cloud layer with very small variation in the vertical. For the same case, the decaying scalar sampling and the JPD-based method show variation of the updraft top-hat term with height with a region of adjustment from the subcloud to the cloud layer.

Often flux decompositions in cumulus cloud layers label the complement of the updraft region as the "environment." However, the results of the JPD-based method show that the downdraft top-hat term can be important. For the present cumulus case there is a (perhaps fortuitous) cancelation of the downdraft top-hat and the within-region updraft covariance terms. The partition of the flow into updraft and environment in the cloud layer obscures the full character of the convection, since downdrafts are incorrectly combined with the environment.

The flux decomposition depends on the thermodynamic variable and the convection type. For the shallow cumulus case the vertical flux of total water mixing ratio and liquid water potential temperature show small differences, but for the stratocumulus case the differences are larger. The dependence of the flux decomposition on the scalar variable can be significant for
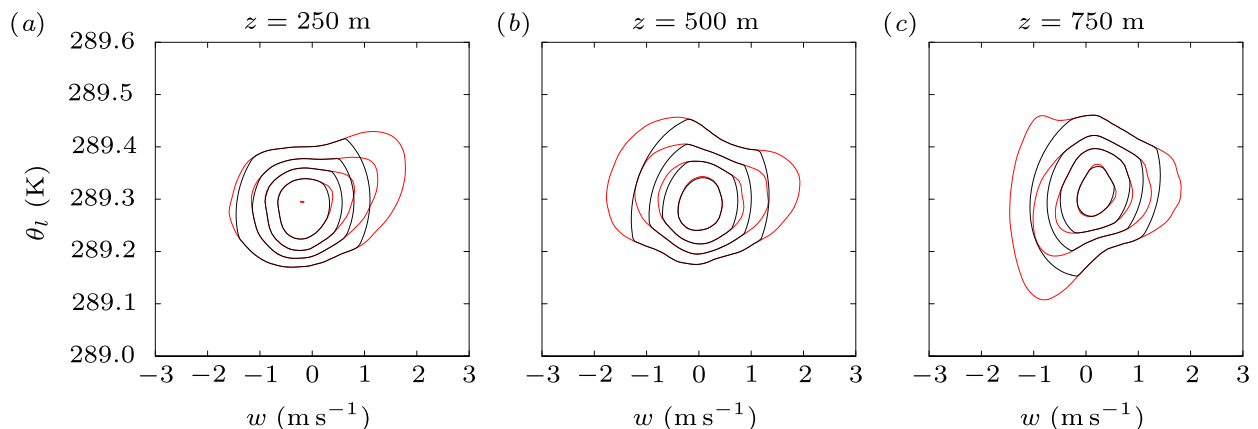

FIG. 14. Joint probability density functions (JPD) of vertical velocity w and liquid water potential temperature θ_l for the DYCOMS II RF01 stratocumulus case at three heights. Red contours correspond to the full JPD and black contours at identical intervals to the joint-Gaussian-based approximation. The contours are logarithmically spaced.
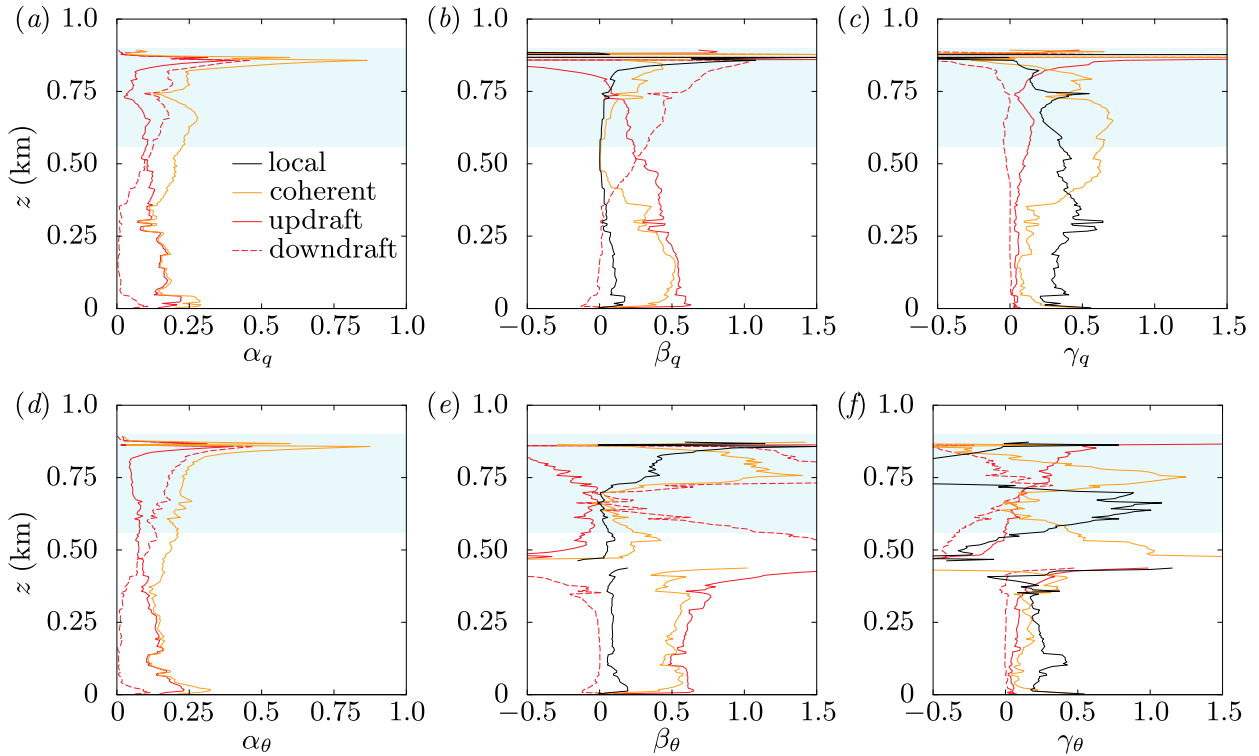
FIG. 15. (top) Vertical flux decomposition for total water mixing ratio and (bottom) liquid water potential temperature for the DYCOMS II RF01 stratocumulus case using the JPD-based method: (a),(d) the area fraction α; (b),(e) the top-hat fraction of the flux β; and (c),(f) the within-subset covariance fraction γ. Two decompositions are used: a local mixing–coherent structures partition and local mixing–updraft–downdraft. The shaded area corresponds to the cloud layer located between 0.56 and 0.90 km.

convection parameterizations, implying that the parameterization must take into account the subtleties of different variables.

APPENDIX

Parameter Sensitivity of Decaying Scalar Conditional Sampling

In the conditional sampling method of Couvreux et al. (2010), the coherent part of the flow consists of all grid cells with positive vertical velocity and scalar concentration $\phi_\alpha > m \times \max(\sigma_\phi, \sigma_{\min})$, where σ_ϕ is the standard deviation of the scalar and $\sigma_{\min}$ a minimum threshold for the standard deviation. In the cloud layer, at z higher than a quarter of the cloud layer depth above the cloud base, the additional condition of positive liquid water content is added, such that only cloudy cells are selected. The results depend on the scaling factor m and the decay time scale τ, which can make the sampling ambiguous.

For cloudy boundary layers, the ambiguity of the conditional sampling can be significantly reduced when m is chosen such that results match the cloud-based sampling. Figure A1 shows the area fraction of the coherent structures diagnosed using the conditional sampling for the shallow cumulus case. The conditional sampling is performed using two scalars with decay times scales of $\tau = 15$ (left) and $\tau = 60$ min
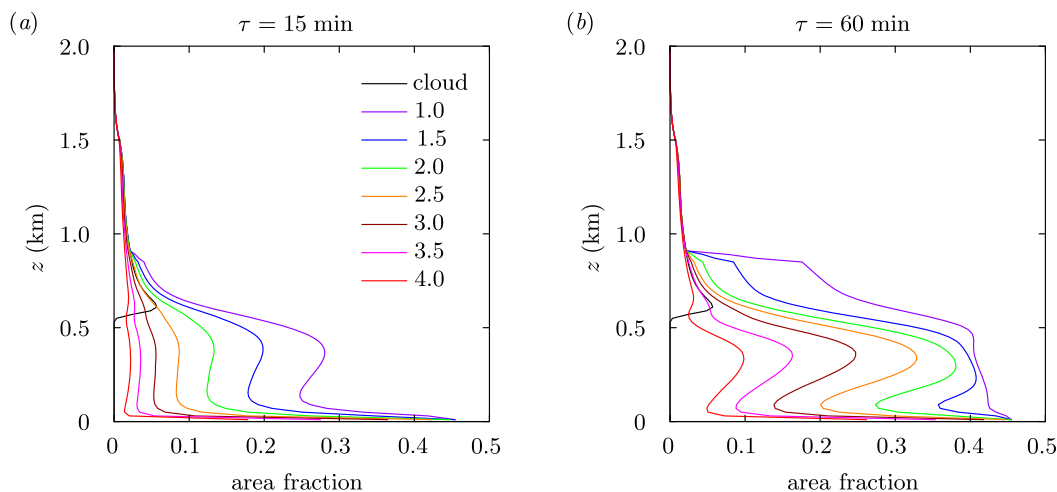
FIG. A1. Area fraction of the coherent structures diagnosed using the conditional sampling method of Couvreux et al. (2010) for the BOMEX shallow cumulus case: (a) $\tau = 15$ and (b) $\tau = 60$ min scalar decay time scales. Colored curves correspond to varying scalar variance threshold factors. The black line is the area fraction of the active cloud, defined as saturated grid cells with positive vertical velocity.

and varying m. The conditional sampling area fraction curves for small m abruptly revert to the cloud fraction curve at $z \approx 0.9$ km when the additional condition of positive cloud liquid water is activated. These results are similar to Fig. 5 of Couvreux et al. (2010). The value of the threshold factor m that matches the cloud sampling at $z \approx 0.9$ km and the variation of the area fraction in the subcloud layer depends on the decay time scale. For the present comparisons the values $\tau = 15$ min and $m = 2.5$ are used because they yield a nearly monotonically decreasing area fraction with a smooth transition to the cloud sampling in the cloud layer.

The selection of τ and m in cloud-free convection is more difficult because a cloud-based sampling is not available to guide the parameter choice. Figure A2 shows the area fraction of the coherent structures diagnosed using the conditional sampling method for the dry convection case. The area fraction dependence on τ and m is similar to the one observed in the subcloud layer of the cumulus convection case (Fig. A1). Without the benefit of matching to cloud fraction, the parameter selection in the dry convective case is somewhat arbitrary. The pair $\tau = 15$ min and $m = 1$ is used based on a similar parameter selection in Couvreux et al. (2010). The area fraction sensitivity diminishes for pairs $\tau = 60$ min and $m < 2$, which can be
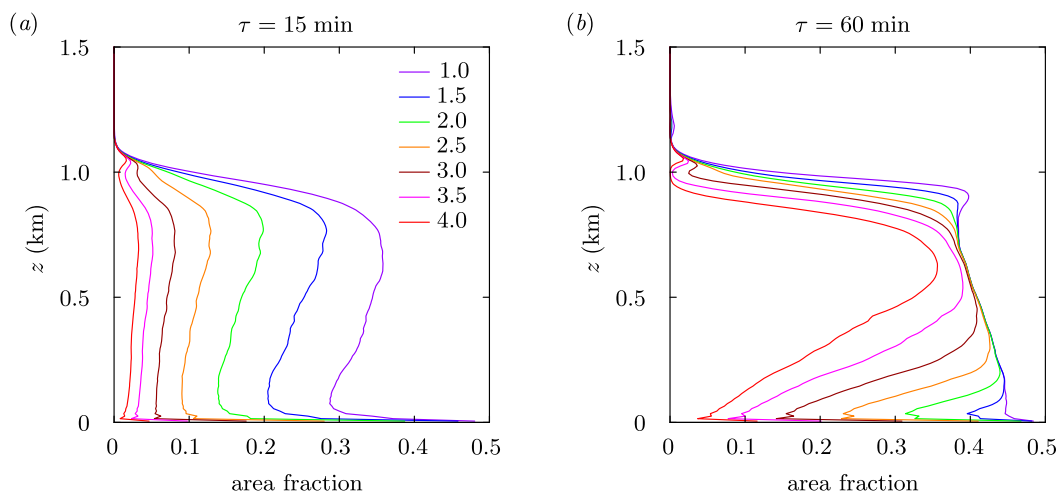

FIG. A2. Area fraction of the coherent structures diagnosed using the conditional sampling method of Couvreux et al. (2010) for the dry convection case: (a) $\tau = 15$ and (b) $\tau = 60$ min scalar decay time scales. Curves correspond to varying scalar variance threshold factors.

another criterion for choosing m and τ. However, $\tau = 60$ min is larger than the time scale of convection for the present conditions (≈ 10 min). Even though the area fraction shows large sensitivity to τ and m, the sensitivity of the flux decomposition is significantly less, similar to the results of the JPD-based method shown in Fig. 7.

REFERENCES

Angevine, W. M., H. Jiang, and T. Mauritsen, 2010: Performance of an eddy diffusivity–mass flux scheme for shallow cumulus boundary layers. *Mon. Wea. Rev.*, **138**, 2895–2912, https://doi.org/10.1175/2010MWR3142.1.

Berg, L. K., and R. B. Stull, 2004: Parameterization of joint frequency distributions of potential temperature and water vapor mixing ratio in the daytime convective boundary layer. *J. Atmos. Sci.*, **61**, 813–828, https://doi.org/10.1175/1520-0469(2004)061<0813:POJFDO>2.0.CO;2.

Bogenschutz, P. A., and S. K. Krueger, 2013: A simplified PDF parameterization of subgrid-scale clouds and turbulence for cloud-resolving models. *J. Adv. Model. Earth Syst.*, **5**, 195–211, https://doi.org/10.1002/jame.20018.

Chatfield, R. B., and R. A. Brost, 1987: A two-stream model of the vertical transport of trace species in the convective boundary layer. *J. Geophys. Res.*, **92**, 13 263–13 276, https://doi.org/10.1029/JD092iD11p13263.

Couvreux, F., F. Guichard, V. Masson, and J.-L. Redelsperger, 2007: Negative water vapour skewness and dry tongues in the convective boundary layer: Observations and large-eddy simulation budget analysis. *Bound.-Layer Meteor.*, **123**, 269–294, https://doi.org/10.1007/s10546-006-9140-y.

——, F. Hourdin, and C. Rio, 2010: Resolved versus parametrized boundary-layer plumes. Part I: A parametrization-oriented conditional sampling in large-eddy simulations. *Bound.-Layer Meteor.*, **134**, 441–458, https://doi.org/10.1007/s10546-009-9456-5.

Golaz, J.-C., V. E. Larson, and W. R. Cotton, 2002: A PDF-based model for boundary layer clouds. Part I: Method and model description. *J. Atmos. Sci.*, **59**, 3540–3551, https://doi.org/10.1175/1520-0469(2002)059<3540:APBMFB>2.0.CO;2.

Holland, J. Z., and E. M. Rasmusson, 1973: Measurements of the atmospheric mass, energy, and momentum budgets over a 500-kilometer square of tropical ocean. *Mon. Wea. Rev.*, **101**, 44–55, https://doi.org/10.1175/1520-0493(1973)101<0044:MOTAME>2.3.CO;2.

Hourdin, F., F. Couvreux, and L. Menut, 2002: Parameterization of the dry convective boundary layer based on a mass flux representation of thermals. *J. Atmos. Sci.*, **59**, 1105–1123, https://doi.org/10.1175/1520-0469(2002)059<1105:POTDCB>2.0.CO;2.

Larson, V. E., and J.-C. Golaz, 2005: Using probability density functions to derive consistent closure relationships among higher-order moments. *Mon. Wea. Rev.*, **133**, 1023–1042, https://doi.org/10.1175/MWR2902.1.

Matheou, G., and D. Chung, 2014: Large-eddy simulation of stratified turbulence. Part II: Application of the stretched-vortex model to the atmospheric boundary layer. *J. Atmos. Sci.*, **71**, 4439–4460, https://doi.org/10.1175/JAS-D-13-0306.1.

——, A. M. Bonanos, C. Pantano, and P. E. Dimotakis, 2010: Large-eddy simulation of mixing in a recirculating shear flow. *J. Fluid Mech.*, **646**, 375–414, https://doi.org/10.1017/S0022112009992965.

——, D. Chung, and J. Teixeira, 2017: Large-eddy simulation of a stratocumulus cloud. *Phys. Rev. Fluids*, **2**, 090509, https://doi.org/10.1103/PhysRevFluids.2.090509.

Neggers, R. A. J., A. P. Siebesma, and H. J. J. Jonker, 2002: A multiparcel model for shallow cumulus convection. *J. Atmos. Sci.*, **59**, 1655–1668, https://doi.org/10.1175/1520-0469(2002)059<1655:AMMFSC>2.0.CO;2.

Pergaud, J., V. Masson, S. Malardel, and F. Couvreux, 2009: A parameterization of dry thermals and shallow cumuli for mesoscale numerical weather prediction. *Bound.-Layer Meteor.*, **132**, 83–106, https://doi.org/10.1007/s10546-009-9388-0.

Randall, D. A., Q. Shao, and C.-H. Moeng, 1992: A second-order bulk boundary-layer model. *J. Atmos. Sci.*, **49**, 1903–1923, https://doi.org/10.1175/1520-0469(1992)049<1903:ASOBBL>2.0.CO;2.

Rio, C., and F. Hourdin, 2008: A thermal plume model for the convective boundary layer: Representation of cumulus clouds. *J. Atmos. Sci.*, **65**, 407–425, https://doi.org/10.1175/2007JAS2256.1.

Romps, D. M., 2010: A direct measure of entrainment. *J. Atmos. Sci.*, **67**, 1908–1927, https://doi.org/10.1175/2010JAS3371.1.

Schumacher, J., 2009: Lagrangian studies in convective turbulence. *Phys. Rev. E*, **79**, 056301, https://doi.org/10.1103/PhysRevE.79.056301.

Siebesma, A. P., and J. W. M. Cuijpers, 1995: Evaluation of parametric assumptions for shallow cumulus convection. *J. Atmos. Sci.*, **52**, 650–666, https://doi.org/10.1175/1520-0469(1995)052<0650:EOPAFS>2.0.CO;2.

——, and Coauthors, 2003: A large eddy simulation intercomparison study of shallow cumulus convection. *J. Atmos. Sci.*, **60**, 1201–1219, https://doi.org/10.1175/1520-0469(2003)60<1201:ALESIS>2.0.CO;2.

——, P. M. M. Soares, and J. Teixeira, 2007: A combined eddy-diffusivity mass-flux approach for the convective boundary layer. *J. Atmos. Sci.*, **64**, 1230–1248, https://doi.org/10.1175/JAS3888.1.

Soares, P. M. M., P. M. A. Miranda, A. P. Siebesma, and J. Teixeira, 2004: An eddy-diffusivity/mass-flux parameterization for dry and shallow cumulus convection. *Quart. J. Roy. Meteor. Soc.*, **130**, 3365–3383, https://doi.org/10.1256/qj.03.223.

Sommeria, G., and J. W. Deardorff, 1977: Subgrid-scale condensation in models of nonprecipitating clouds. *J. Atmos. Sci.*, **34**, 344–355, https://doi.org/10.1175/1520-0469(1977)034<0344:SSCIMO>2.0.CO;2.

Stevens, B., and Coauthors, 2005: Evaluation of large-eddy simulations via observations of nocturnal marine stratocumulus. *Mon. Wea. Rev.*, **133**, 1443–1462, https://doi.org/10.1175/MWR2930.1.

Suselj, K., J. Teixeira, and D. Chung, 2013: A unified model for moist convective boundary layers based on a stochastic eddy-diffusivity/mass-flux parameterization. *J. Atmos. Sci.*, **70**, 1929–1953, https://doi.org/10.1175/JAS-D-12-0106.1.

Wang, S., and B. Stevens, 2000: Top-hat representation of turbulence statistics in cloud-topped boundary layers: A large eddy simulation study. *J. Atmos. Sci.*, **57**, 423–441, https://doi.org/10.1175/1520-0469(2000)057<0423:THROTS>2.0.CO;2.

Williams, A. G., and J. M. Hacker, 1992: The composite shape and structure of coherent eddies in the convective boundary layer. *Bound.-Layer Meteor.*, **61**, 213–245, https://doi.org/10.1007/BF02042933.

Willis, G. E., and J. W. Deardorff, 1974: A laboratory model of the unstable planetary boundary layer. *J. Atmos. Sci.*, **31**, 1297–1307, https://doi.org/10.1175/1520-0469(1974)031<1297:ALMOTU>2.0.CO;2.

Wyngaard, J. C., and C.-H. Moeng, 1992: Parameterizing turbulent diffusion through the joint probability density. *Bound.-Layer Meteor.*, **60**, 1–13, https://doi.org/10.1007/BF00122059.

Young, G. S., 1988: Turbulence structure of the convective boundary layer. Part II: Phoenix 78 aircraft observations of thermals and their environment. *J. Atmos. Sci.*, **45**, 727–735, https://doi.org/10.1175/1520-0469(1988)045<0727:TSOTCB>2.0.CO;2.